Chinese Journal of Natural Medicines

Nephropathy 1 Formula alleviates kidney injury by ameliorating mitochondrial dysfunction and pyroptosis in diabetic nephropathy through the TMAO–mROS–NLRP3 axis

Tingting Wei, Yujiu Gao, Liting Zhu, Congcong Zeng, Rui Cai, Fu Rao, Yue Zhao, Xiaochun Zhang, Jiashun Yang, Yinrui Sheng, Zhengzhong Yuan, Jinguo Cheng

Citation: Tingting Wei, Yujiu Gao, Liting Zhu, Congcong Zeng, Rui Cai, Fu Rao, Yue Zhao, Xiaochun Zhang, Jiashun Yang, Yinrui Sheng, Zhengzhong Yuan, Jinguo Cheng, Nephropathy 1 Formula alleviates kidney injury by ameliorating mitochondrial dysfunction and pyroptosis in diabetic nephropathy through the TMAO–mROS–NLRP3 axis, Chinese Journal of Natural Medicines, 2026, 24(4), 454–469. doi: 10.1016/S1875–5364(26)61174–0.

View online: https://doi.org/10.1016/S1875–5364(26)61174–0

Wechat

Chinese Journal of Natural Medicines 24 (2026) 454-469

Contents lists available at ScienceDirect

Chinese Journal of Natural Medicines

journal homepage: www.cjnmcpu.com/

Original article

Nephropathy 1 Formula alleviates kidney injury by ameliorating mitochondrial dysfunction and pyroptosis in diabetic nephropathy through the TMAO-mROS-NLRP3 axis

Tingting Wei[a,b,Δ], Yujiu Gao[b,d,Δ], Liting Zhu[b,c], Congcong Zeng[b,c], Rui Cai[c], Fu Rao[c], Yue Zhao[c], Xiaochun Zhang[c], Jiashun Yang[c], Yinrui Sheng[c], Zhengzhong Yuan[b,c,*], Jinguo Cheng[b,c,*]

[a] *Laboratory Animal Centre*, *Wenzhou Medical University*, *Wenzhou 325035*, *China*
[b] *Department of Traditional Chinese Medicine*, *First Affiliated Hospital of Wenzhou Medical University*, *Wenzhou 325035*, *China*
[c] *School of Chinese Medicine*, *Wenzhou Medical University*, *Wenzhou 325035*, *China*
[d] *Hubei Key Laboratory of Embryonic Stem Cell Research*, *Hubei Provincial Clinical Research Center for Umbilical Cord Blood Hematopoietic Stem Cells*, *Department of Nephrology*, *Taihe Hospital*, *Hubei University of Medicine*, *Shiyan 442000*, *China*

ARTICLE INFO

Article history:
Received 28 June 2025
Revised 1 September 2025
Accepted 18 October 2025
Available online 20 April 2026

Keywords:
Diabetic nephropathy
Trimethylamine-*N*-oxide (TMAO)
Mitochondrial dysfunction
Pyroptosis

ABSTRACT

Nephropathy 1 Formula (N1F), a traditional Chinese medicine (TCM), has demonstrated promising clinical efficacy in diabetic nephropathy (DN). However, its underlying protective mechanisms remain insufficiently defined. In this study, a type 2 diabetes mellitus (T2DM) mouse model was established using a high-fat diet (HFD) and streptozotocin (STZ). Additionally, DN was simulated *in vitro via* exposure of mouse glomerular mesangial cells (MES-13) to high glucose (HG) and trimethylamine-*N*-oxide (TMAO). To elucidate the mechanistic basis of N1F's renoprotective effects, an integrative approach combining metabolomics, transcriptomics, and 16S ribosomal ribonucleic acid (rRNA) gene sequencing was employed. N1F treatment reduced the urinary albumin-to-creatinine ratio (UACR), preserved renal function, and attenuated histopathological damage and renal fibrosis in diabetic mice. Mechanistically, N1F modulated systemic TMAO levels and energy metabolism, altered gut microbiota composition, and suppressed microbial production of TMAO-related metabolites. Under hyperglycemic conditions, TMAO induced excessive mitochondrial reactive oxygen species (mROS), impaired mitochondrial dynamics, and disrupted cellular energy metabolism. In contrast, N1F normalized mROS levels, restored mitochondrial structure and function, enhanced oxidative phosphorylation (OXPHOS), increased ATP production, and reduced glycolytic dependency. Furthermore, N1F downregulated the expression of key pyroptosis-related proteins—including NOD-like receptor family pyrin domain-containing 3 (NLRP3), *N*-terminal gasdermin D (GSDMD), cleaved-Casp1, interleukin-1β (IL-1β), and IL-18—in both *in vivo* and *in vitro* models, indicating suppression of pyroptosis *via* inhibition of the TMAO-mROS-NLRP3 signaling axis. Collectively, these findings demonstrate that N1F exerts protective effects against DN by targeting mitochondrial dysfunction and pyroptotic injury, supporting its potential as a therapeutic strategy for DN.

1. Introduction

Diabetic nephropathy (DN), a major microvascular complication of diabetes mellitus (DM), is a leading cause of end-stage renal disease (ESRD) globally [1]. Despite advances in glycemic and blood pressure control, the incidence of DN continues to rise, indicating that additional pathological mechanisms operate beyond conventional metabolic dysregulation [2–4]. Accumulating evidence implicates mitochondrial dysfunction, oxidative stress, and chronic inflammation as central contributors to DN progression [5], underscoring the need for novel therapeutic strategies.

Metabolomics, a systems biology approach that profiles endogenous metabolites under pathological conditions, has provided critical insights into metabolic perturbations in DN. These include dysregulation of glucose, lipid, and energy metabolism, as well as methylamine pathways and oxidative stress responses [6, 7]. Among these alterations, gut-derived uremic toxins have emerged as key mediators of DN pathogenesis. The gut–kidney axis links intestinal microbiota to renal function through microbial metabolites such as *p*-cresyl sulfate (PCS), indoxyl sulfate (IS), phenyl sulfate (PS), and trimethylamine *N*-oxide (TMAO) [8]. TMAO is produced from dietary choline and L-carnitine *via* gut microbial conversion to trimethylamine (TMA), which is subsequently oxidized in the liver by flavin monooxygenase 3 (FMO3) [9]. Elevated circulating TMAO levels are observed in both patients with DN and diabetic animal models, where they exacerbate renal injury by promoting fibrosis, inflammation, and functional decline [10, 11]. Mechanistically, TMAO impairs oxidative phosphorylation (OXPHOS), reduces ATP production, disrupts calcium homeostasis, and induces accumulation of mitochondrial reactive oxygen species (mROS)—hallmarks of mitochondrial dysfunction [12]. Increased mROS activate the NOD-like receptor family pyrin domain-containing 3 (NLRP3) inflammasome, trig-

* Corresponding author.
E-mail addresses: wzyzz2008@126.com (Z. Yuan); wzchengjinguo@126.com (J. Cheng)
Δ These authors contributed equally to this work.

https://doi.org/10.1016/S1875-5364(26)61174-0

gering pyroptosis, an inflammatory form of programmed cell death implicated in DN progression [13, 14].

Mitochondria serve as central regulators of cellular energy metabolism and redox balance and are essential for maintaining renal function. In energy-demanding organs like the kidney, mitochondria generate ATP primarily through the tricarboxylic acid (TCA) cycle, OXPHOS, and fatty acid oxidation [15–17]. Mitochondrial integrity relies on dynamic processes including fusion, fission, and biogenesis [18, 19]. In DN, persistent hyperglycemia leads to mitochondrial fragmentation, suppressed biogenesis, and excessive mROS generation [20, 21]. Dysfunctional mitochondria amplify oxidative stress and pro-inflammatory signaling, contributing to podocyte injury, endothelial dysfunction, and irreversible renal damage [22, 23]. Therefore, restoring mitochondrial homeostasis and limiting mROS production represent promising therapeutic avenues for slowing DN progression.

Pyroptosis plays a pivotal role in DN-associated inflammation and tubulointerstitial injury. It is initiated by activation of the NLRP3 inflammasome, resulting in caspase-1 (casp1)-mediated cleavage of gasdermin D (GSDMD) and formation of plasma membrane pores. This process culminates in the release of pro-inflammatory cytokines, including interleukin-1β (IL-1β) and IL-18 [24, 25]. NLRP3-driven pyroptosis has been documented in podocytes in db/db and streptozotocin (STZ)-induced diabetic mouse models, and genetic ablation of NLRP3 confers renoprotection [26, 27]. Hyperglycemia and elevated free fatty acid levels initiate this pyroptotic cascade *via* pattern recognition receptor (PRR) activation and mROS accumulation [28, 29]. In turn, mROS further compromise mitochondrial integrity, propagating pyroptotic signaling in glomerular and tubular cells and accelerating DN progression [30-32]. Thus, targeting the TMAO-mROS-NLRP3 signaling axis may effectively suppress pyroptosis and mitigate DN progression.

Traditional Chinese medicine (TCM), with its holistic and multitargeted therapeutic philosophy, offers potential interventions for DN [33]. At the single-herb level, individual components exhibit specific pharmacological properties. For instance, Astragali Radix modulates glucose and lipid metabolism and ameliorates DN features such as hyperglycemia, proteinuria, and glomerular hyperfiltration [34], while *Rheum officinale* demonstrates anti-fibrotic effects in various kidney injury models [35]. Polyherbal formulations often yield enhanced efficacy through synergistic interactions. The Huanglian Jiedu Decoction exemplifies this principle, combining *Coptis chinensis* (hypolipidemic), *Scutellaria baicalensis* (hemodynamic regulation), *Gardenia jasminoides* (anti-inflammatory), and *Phellodendron amurense* (detoxification), collectively activating the AGE/RAGE/AKT/Nrf2 pathway to counteract DN progression [36]. Nephropathy 1 Formula (Modified Liujunzi Decoction, N1F), a modified version of the classical Liujunzi Decoction, contains 13 herbs traditionally used to tonify the spleen and kidney, eliminate turbidity, and promote blood circulation. Clinically, N1F has shown beneficial effects in DN patients and reduces renal interstitial fibrosis [37]. Nevertheless, its underlying molecular mechanisms remain poorly understood.

To address this knowledge gap, we employed an integrative multi-omics strategy—including metabolomics, transcriptomics, and gut microbiota profiling—combined with *in vivo* and *in vitro* models of DN. We hypothesized that N1F ameliorates DN by targeting the TMAO-mROS-NLRP3 signaling axis, thereby improving mitochondrial function and suppressing pyroptosis. This study elucidates the mechanistic basis of N1F's therapeutic effects and supports its development as a novel intervention for DN.

2. Materials and methods

2.1. N1F preparation

N1F comprises 13 traditional Chinese medicinal herbs: 12 g of Bupleuri Radix, 10 g of Cortex Phellodendron, 6 g of Rhei Radix et Rhizoma, 6 g of Radix Aconiti Lateralis Preparata, 12 g of Ramulus Cinnamomi, 15 g of Eupolyphaga Seu Steleophaga/Steleophaga, 12 g of Wenyujin Concisum Rhizoma, 30 g of Actinidia Valvatae Radix, 12 g of Carapax Trionycis (vinegar-processed), 30 g of Folium Cycas Revoluta, 12 g of Notoginseng Radix, 30 g of Codonopsis Radix, and 30 g of Astragali Radix. Raw materials were obtained from the Pharmacy Department of the First Affiliated Hospital of Wenzhou Medical University (WMU) and authenticated by Prof. Xiaocheng Chen (WMU). The mixture was soaked in 1 L of double-distilled water and extracted by decoction for 2 h using a maceration method. The extract was filtered and concentrated *via* rotary evaporation under reduced pressure at 60 °C. The final concentrate was adjusted to three concentrations (1.235, 2.47, and 4.94 $g \cdot mL^{-1}$) based on crude drug content, according to human-to-animal dose conversion normalized by body surface area. The decoction was sealed and stored at −20 °C in the dark until use.

2.2. N1F drug-containing serum preparation

To prepare N1F-containing serum for cellular experiments, serum was collected from rats administered the N1F decoction. Twenty male Sprague-Dawley (SD) rats were randomly divided into two groups (n = 10 per group): control and N1F-treated. Based on human-to-rat dose conversion, the N1F group received 19.38 $g \cdot kg^{-1} \cdot d^{-1}$ of decoction *via* oral gavage, while the control group received an equivalent volume of normal saline for seven consecutive days. 2 h after the final administration, rats were anesthetized, and blood was collected *via* abdominal aorta puncture. Blood samples were centrifuged at 3000 $r \cdot min^{-1}$ for 15 min at 4 °C to obtain control and N1F-treated serum. The sera were heat-inactivated at 56 °C for 30 min, filtered through a 0.22 μm microporous membrane, and stored at −20 °C until use.

2.3. Ultra-high performance liquid chromatography-tandem mass spectrometry (UPLC-MS/MS) analysis of N1F absorbed into blood

An aliquot of 50 μL of N1F-containing serum was transferred to a 1.5 mL centrifuge tube, and 300 μL of 20% acetonitrile/methanol extraction solution containing an internal standard was added. The internal standard stock solution (1000 $\mu g \cdot mL^{-1}$) was prepared by dissolving 1 mg of the reference compound in 1 mL of 20% acetonitrile/methanol and diluted to a working concentration of 250 $\mu g \cdot mL^{-1}$. The mixture was vortexed for 3 min and then centrifuged at 12 000 $r \cdot min^{-1}$ for 10 min at 4 °C. Subsequently, 200 μL of the supernatant was transferred to a fresh 1.5 mL centrifuge tube and incubated at −20 °C for 30 min, followed by a second centrifugation at 12 000 $r \cdot min^{-1}$ for 3 min at 4 °C. Finally, 180 μL of the supernatant was transferred to an autosampler vial for UPLC-MS/MS analysis.

2.4. Animal model and administration

Male C57BL/6J mice (6 weeks old, 20–24 g) were purchased from Beijing Vital River Laboratory Animal Technology Co., Ltd. (Beijing, China). All animals were housed under specific pathogen-free (SPF) conditions at the Laboratory Animal Center of WMU (Wenzhou, China), with controlled temperature (22 ± 2 °C), humidity (50%–60%), and a 12-h light/dark cycle. Mice had free access to standard chow and tap water ad libitum. All procedures were approved by the Institutional Animal Care and Use Committee of WMU and conducted in accordance with the Guide for the Care and Use of Laboratory Animals. All animal experiments were conducted with approval from the Ethics Committee of WMU (No. wydw2022-0633) on 9rd March, 2022.

Type 2 DM (T2DM) was induced by feeding mice a high-fat diet (HFD) for 6 weeks. After a 12-h fast, STZ (40 $mg \cdot kg^{-1}$) in citrate buffer (pH 4.5) was administered *via* intraperitoneal injection daily for five consecutive days. 72 h after the last injection, fasting blood glucose levels were measured from tail vein blood using a Roche glucometer. Mice exhibiting fasting blood glucose

levels exceeding 11.1 mmol·L^{-1} across three consecutive measurements were considered diabetic and assigned to one of five HFD-fed groups: Model group (MOD; physiological saline), Positive control group (Met; metformin hydrochloride, 250 mg·kg^{-1}·d^{-1}), N1F high-dose group (N1F-H; 56.44 g·kg^{-1}·d^{-1}), N1F medium-dose group (N1F-M; 28.22 g·kg^{-1}·d^{-1}), and N1F low-dose group (N1F-L; 14.11 g·kg^{-1}·d^{-1}). Age-matched control mice fed a standard diet received physiological saline (Con group). All treatments were administered *via* oral gavage for 10 weeks. Body weight, fasting blood glucose, food intake, and water intake were recorded weekly. Urine was collected over 12 h using metabolic cages. Blood samples were collected from the orbital sinus, and fecal samples were obtained directly from the colon. Following euthanasia *via* CO_2 asphyxiation, kidney tissues were immediately harvested. Samples—including blood, urine, feces, and kidneys—were stored at −80 °C for subsequent analysis.

2.5. Nuclear magnetic resonance (NMR) metabolomic analysis

^{1}H NMR spectra were acquired at 25 °C using a Bruker AVANCE III 600 MHz NMR spectrometer equipped with a triple-resonance probe and z-axis pulsed field gradient (Bruker BioSpin, Rheinstetten, Germany). Frozen kidney tissues were placed in centrifuge tubes and homogenized in ice-cold methanol (1 g∶4 mL) and distilled water (1 g∶0.85 mL) at 4 °C, followed by vortexing for 15 sec. Ice-cold chloroform and distilled water were then added (1 g∶2 mL), and the mixture was vortexed again for 15 sec. The sample was incubated on ice for 15 min and centrifuged at 10 000 × *g* for 15 min at 4 °C. The supernatant was collected and lyophilized for approximately 24 h. Dried extracts were reconstituted in 500 μL of D_2O containing 0.25 mmol·L^{-1} sodium trimethylsilyl propionate-d_4 (TSP) and transferred to 5 mm NMR tubes. NMR spectra were acquired using a one-dimensional ZGPR pulse sequence with water suppression. Spectral parameters included: spectral width = 12 000 Hz; data points = 256 K; relaxation delay = 4 s; acquisition time = 2.66 s per scan.

Urine samples were thawed, and 200 μL aliquots were mixed with 50 μL of D_2O containing 0.36 mmol·L^{-1} TSP and 300 μL phosphate buffer (PB, 0.2 mol·L^{-1} Na_2HPO_4/NaH_2PO_4, pH 7.4). The mixture was centrifuged, and 500 μL of the supernatant was loaded into a 5 mm NMR tube. ^{1}H NMR spectra were acquired using a one-dimensional NOESY pulse sequence with water suppression. Acquisition parameters were identical to those used for kidney samples.

Approximately 0.1 g of fecal sample was weighed and suspended in phosphate-buffered saline (PBS, 1 g∶2 mL). The suspension was vortexed until fully dispersed and incubated on ice for 10 min. After centrifugation at 10 000 × *g* for 10 min at 4 °C, 100 μL of the supernatant was transferred to a new tube and combined with 400 μL of D_2O containing 0.1 mmol·L^{-1} TSP. The mixture was vortexed for 15 sec and centrifuged again at 12 000 × *g* for 10 min at 4 °C. The resulting supernatant was transferred to a 5 mm NMR tube. Spectra were acquired using the ZGPR pulse sequence with the same parameters as above.

All NMR spectra were manually phase- and baseline-corrected and referenced to the TSP signal at 0 using Topspin 3.0 software (Bruker Biospin, Rheinstetten, Germany). To evaluate metabolic differences among groups, partial least squares-discriminant analysis (PLS-DA) was performed on Pareto-scaled NMR data using SIMCA 12.0 software (Umetrics, Umeå, Sweden). Model performance was assessed using leave-one-out cross-validation and permutation testing.

2.6. Targeted metabolic analysis of TMAO and TMA

Targeted quantification of TMAO and TMA in plasma was performed using a SHIMADZU CBM-30A Lite UHPLC system coupled to an API 4500 QTRAP mass spectrometer (AB SCIEX, Foster City, CA, USA) in positive electrospray ionization (ESI) mode. The injection volume was 2 μL, and the column temperature was maintained at 45 °C. Collision-induced dissociation was conducted at a collision energy of 40 V. The mobile phase consisted of 0.1% formic acid in water (A) and acetonitrile (B). Gradient elution was programmed as follows: 0–4 min, 10%–40% B; 4–10 min, 40%–90% B; 10–12 min, 90%–10% B. Data were acquired in multiple reaction monitoring (MRM) mode using Analyst software (version 2.6).

2.7. Biochemical indicators and histopathology changes

Serum creatinine (SCR), urinary albumin-to-creatinine ratio (UACR), alanine aminotransferase (ALT), and aspartate aminotransferase (AST) levels were determined using a fully automatic biochemical analyzer (AU480, Beckman Coulter, USA).

Kidney tissues were collected at sacrifice and fixed in 10% paraformaldehyde for 24 h. Fixed tissues were embedded in paraffin and sectioned at 2 μm thickness. Sections were stained with hematoxylin and eosin (H&E), periodic acid–Schiff (PAS), and Masson's trichrome for morphological assessment.

2.8. Mitochondrial ultrastructure

Mitochondrial ultrastructure in kidney tissue was examined using transmission electron microscopy (TEM) at Wuhan Servicebio Technology Co., Ltd. (Wuhan, China). Specimens were fixed with a TEM-specific fixative (Fixative for TEM G1102, Wuhan Servicebio Technology Co., Ltd., Wuhan, China) at 4 °C overnight. After fixation, specimens were rinsed three times with 0.1 mol·L^{-1} PB (pH 7.4), then incubated in the dark at room temperature with 1% OsO_4 for 2 h. Following removal of OsO_4, specimens were washed three times with 0.1 mol·L^{-1} PB. Dehydration was carried out using a graded ethanol series, followed by resin infiltration and embedding in EMBed 812 at 37 °C overnight. Embedded specimens were cured at 60 °C for 48 h. Ultrathin sections (60–80 nm) were cut using an ultramicrotome (Leica UC7, Leica Company, Germany). Sections were stained with saturated alcohol solutions of 2% uranium acetate and 2.6% lead citrate in the dark and allowed to dry overnight at room temperature. Stained sections were visualized using TEM (Hitachi HT7800, Hitachi Company, Tokyo, Japan).

2.9. 16S ribosomal ribonucleic acid (rRNA) sequencing

Bacterial genomic deoxyribonucleic acid (DNA) was extracted using the DNeasy PowerSoil Pro Kit (Qiagen, CA, USA). DNA quality and concentration were evaluated using a NanoDrop spectrophotometer (Thermo Fisher Scientific, MA, USA) and agarose gel electrophoresis. The V3–V4 hypervariable regions of the 16S rRNA gene were amplified using primers 343F (5′-TACGGRAGGCAGCAG-3′) and 798R (5′-AGGGTATCTAATCCT-3′). After polymerase chain reaction (PCR) amplification, products were purified and quantified prior to library construction. Sequencing was performed on an Illumina NovaSeq 6000 platform (Illumina Inc., CA, USA). All sequencing and bioinformatic analyses were conducted in collaboration with Nanjing Personal Biotechnology Co., Ltd. (Nanjing, China).

2.10. Immunohistochemistry

Kidney tissues were fixed in 10% neutral-buffered formalin for 24 h and embedded in paraffin. Paraffin-embedded tissues were sectioned at 4 μm and incubated with primary antibodies (Boster, Wuhan, China), followed by horseradish peroxidase (HRP)-conjugated secondary antibodies (Beyotime, Shanghai, China). Antibody binding was detected using 3,3′-diaminobenzidine (DAB; Beyotime).

2.11. Cell culture and treatment

Mouse glomerular mesangial cells (MES-13, iCell Bioscience)

were cultured in DMEM/F12 (1∶1) medium supplemented with 10% fetal bovine serum (FBS) and 1% penicillin–streptomycin at 37 °C in a humidified incubator with 5% CO_2. To establish an *in vitro* disease model, MES-13 cells were exposed to high glucose (25 mmol·L^{-1}) and TMAO (400 μmol·L^{-1}). Intervention groups were treated with MCC950 (10 μmol·L^{-1}, Sigma-Aldrich), Mito-TEMPO (100 μmol·L^{-1}, Sigma-Aldrich), or 6% N1F-containing serum for 24 h. Cells were allocated into nine groups: Con, HG, TMAO, HG + TMAO, N1F, MitoTEMPO, N1F + MitoTEMPO, MCC950, and N1F + MCC950. Group assignments were adjusted according to experimental design and preliminary results. Cell viability was assessed using a cell counting kit-8 (CCK-8; Elabscience) following the manufacturer's instructions.

2.12. mROS detection

mROS levels in MES-13 cells were measured using the MitoSOX™ Red mitochondrial superoxide indicator (S0061S, Beyotime, China), according to the manufacturer's protocol.

2.13. Enzyme-linked immunosorbent assay (ELISA) analysis

IL-18 (AB-K106402, Abmart, China) and IL-1β (AB-K156302, Abmart, China) levels were quantified using ELISA kits following the manufacturer's instructions.

2.14. Mitochondrial membrane potential study

Mitochondrial membrane potential (Δψm) was assessed using JC-1 dye (C2003S, Beyotime, China) with Hoechst 33342 nuclear staining (C1022, Beyotime, China). After treatment, cells were washed once with PBS. Then, 1 mL of JC-1 working solution was added to each well, mixed gently, and incubated at 37 °C for 20 min in a humidified incubator. After incubation, the staining solution was removed, and cells were washed with PBS to remove excess dye. Hoechst 33342 (5 μg·mL^{-1}) was added and incubated at room temperature for 10 min in the dark. Cells were visualized under a fluorescence microscope (TI-S, Nikon, Japan). JC-1 aggregates in healthy mitochondria emit red fluorescence, whereas monomers in depolarized mitochondria emit green fluorescence, indicating loss of mitochondrial membrane potential. Hoechst 33342-stained nuclei exhibit blue fluorescence.

2.15. ATP quantification

ATP levels were measured using an ATP content assay kit (S0027, Beyotime, China), following the manufacturer's instructions. Cells were lysed in lysis buffer and centrifuged at 12 000 × *g* for 5 min at 4 °C. The supernatant was collected and mixed with ATP detection reagent. A standard curve was generated by measuring relative luminescence units (RLU) using a chemiluminescence instrument (ChemiDoc, Bio-Rad, USA), allowing ATP concentrations to be calculated based on the standard curve.

2.16. Oxygen consumption rate (OCR) and extracellular acidification rate (ECAR)

OCR and ECAR were measured using a Seahorse XF96 Extracellular Flux Analyzer (Agilent Technologies, USA) according to the manufacturer's protocol. MES-13 cells were seeded in XF96 microplates at 80 000 cells/well. For OCR measurement, cells were incubated in assay medium containing 2 mmol·L^{-1} GlutaMAX, 2.5 mmol·L^{-1} sodium pyruvate, and 10 mmol·L^{-1} glucose. Mitochondrial respiration was assessed by sequential injection of 1 μmol·L^{-1} oligomycin, 2 μmol·L^{-1} carbonyl cyanide 4-(trifluoromethoxy) phenylhydrazone (FCCP), 1 μmol·L^{-1} rotenone, and 1 μmol·L^{-1} antimycin A. Maximal OCR was calculated as the difference between FCCP-stimulated OCR and non-mitochondrial OCR (after rotenone and antimycin A addition). For ECAR analysis, 10 mmol·L^{-1} glucose, 1 μmol·L^{-1} oligomycin, and 42.5 mmol·L^{-1} 2-deoxy-D-glucose (2-DG) were sequentially added to the cells.

2.17. Messenger RNA (mRNA) isolation and real-time quantitative PCR (RT-qPCR)

Total RNA was extracted from renal tissues or cells using TRIzol reagent (15596018CN, Invitrogen, USA) according to the manufacturer's instructions. RNA was reverse transcribed using HiScript IV All-in-One Ultra RT SuperMix for qPCR (R433–01, Vazyme, Nanjing, China). RT-qPCR was performed using a Real-Time Fluorescence Quantitative PCR instrument (CFX384, Bio-Rad, USA) and ChamQ Universal SYBR qPCR Master Mix (R711-02, Vazyme Biotech Co., Ltd.). Relative mRNA expression levels were calculated using the $2^{-\Delta\Delta Ct}$ method and normalized to *Gapdh* expression. Primer sequences are listed in Supporting Table 1.

2.18. Western blotting

Proteins were extracted from renal tissues and renal epithelial cells. Equal amounts of protein (20–30 μg) were separated by SDS-PAGE and transferred to PVDF membranes. Membranes were blocked with 5% skim milk in TBST for 2 h at room temperature and incubated overnight at 4 °C with primary antibodies against transforming growth factor β (TGF-β), *α*-smooth muscle actin (*α*-SMA), NLRP3, *N*-terminal GSDMD (*N*-GSDMD), cleaved-casp1, cleaved-IL-1β, IL-18, ATP5A1, SDHB, UQCRC2, mitochondrial fusion protein mitofusin-2 (Mfn2), and Fis1. After washing, membranes were incubated with HRP-conjugated secondary antibodies at 37 °C for 1.5 h. Signals were developed using enhanced chemiluminescence (ECL, SQ203L, EpiZyme, China). Band intensities were quantified using ImageJ [National Institutes of Health (NIH), Bethesda, MD, USA]. Detailed antibody information, including dilutions, is provided in Supporting Table 2.

2.19. Statistical analysis

Statistical analyses were conducted using GraphPad Prism software version 10.1.2. Differences among groups were analyzed by one-way ANOVA followed by Dunnett's test. Data are presented as mean ± SD. Tests were two-sided, with statistical significance defined as $P < 0.05$. Significance levels are denoted as follows: $^{*}P < 0.05$, $^{**}P < 0.01$, $^{***}P < 0.001$, and $^{****}P < 0.0001$.

3. Results

3.1. Identification of N1F absorbed into blood by UPLC-MS/MS

The UPLC-MS/MS method was employed to identify absorbable components of N1F. Total ion current chromatograms of blank serum and N1F drug-containing serum are presented in Figs. 1A and 1B, respectively. A total of 1088 chemical constituents were detected in the serum, with relative abundances of compound categories shown in Fig. 1C. Kyoto Encyclopedia of Genes and Genomes (KEGG) pathway enrichment analysis was performed on differentially abundant components between blank serum and N1F drug-containing serum (Fig. 1D). After de-duplication, the top 25 absorbable compounds from N1F were identified (Supporting Table 3), including rhein, scutellarin, liquiritigenin, codonopsinol A, and emodin.

3.2. N1F improved kidney dysfunction and alleviated renal injury in T2DM mice

To evaluate the renoprotective effects of N1F in DN, a T2DM

mouse model was established using a HFD combined with STZ injection, followed by oral administration of N1F at various doses for 10 weeks (Fig. 2A). Treatment with different doses of N1F significantly reduced fasting blood glucose levels and lowered SCR and UACR (Fig. 2B). Histological evaluation *via* H&E and PAS staining revealed that N1F attenuated glomerular mesangial cell proliferation and matrix expansion in T2DM mice (Fig. 2C). Masson trichrome staining showed marked renal fibrosis in T2DM mice, which was dose-dependently ameliorated by N1F treatment (Fig. 2C). Western blotting analysis demonstrated that N1F significantly downregulated *α*-SMA and TGF-β1 expression in renal tissues (Figs. 2D and 2E), indicating suppression of renal fibrosis. These results indicate that high-dose N1F exerts protective effects against kidney dysfunction and renal injury in diabetic mice, thereby delaying DN progression.

3.3. N1F regulated TMAO metabolism and energy metabolism in T2DM mice

Although N1F has been shown to protect renal function, its underlying mechanism remains unclear. Previous studies have linked metabolic disturbances to renal injury in T2DM mice, identifying metabolites that may influence renal function [6, 38]. To investigate the metabolic mechanisms underlying N1F action, a ^{1}H NMR-based metabolomics approach and targeted MS analysis were applied. Representative ^{1}H NMR spectra from kidney samples are shown in Fig. 3A. In total, 26 metabolites were identified in the NMR-based metabolome, including energy metabolism–related metabolites (succinate, fumarate, creatinine, lactate, glucose, and maltose), TMAO metabolism–related metabolites (choline, TMA, and TMAO), amino acids (leucine, isoleucine, alanine, glutamate, aspartate, taurine, glycine, and phenylalanine), nucleotide metabolism–related metabolites (uracil and uridine), and other metabolites (3-HB, acetate, GPC, myo-inositol, inosine, niacinamide, and anserine). Representative ^{1}H NMR spectra from urine and fecal samples are provided in Supporting Figs. 1A and 2A.

Furthermore, PLS-DA was conducted to assess metabolic shifts among the Con, Mod, and N1F-H groups and to identify discriminating metabolites. The PLS-DA score plots of kidney, urine, and fecal samples showed clear separations across the three groups (Fig. 3B, Supporting Figs. 1B and 2B). These findings were validated by permutation tests (Fig. 3C, Supporting Figs. 1C and

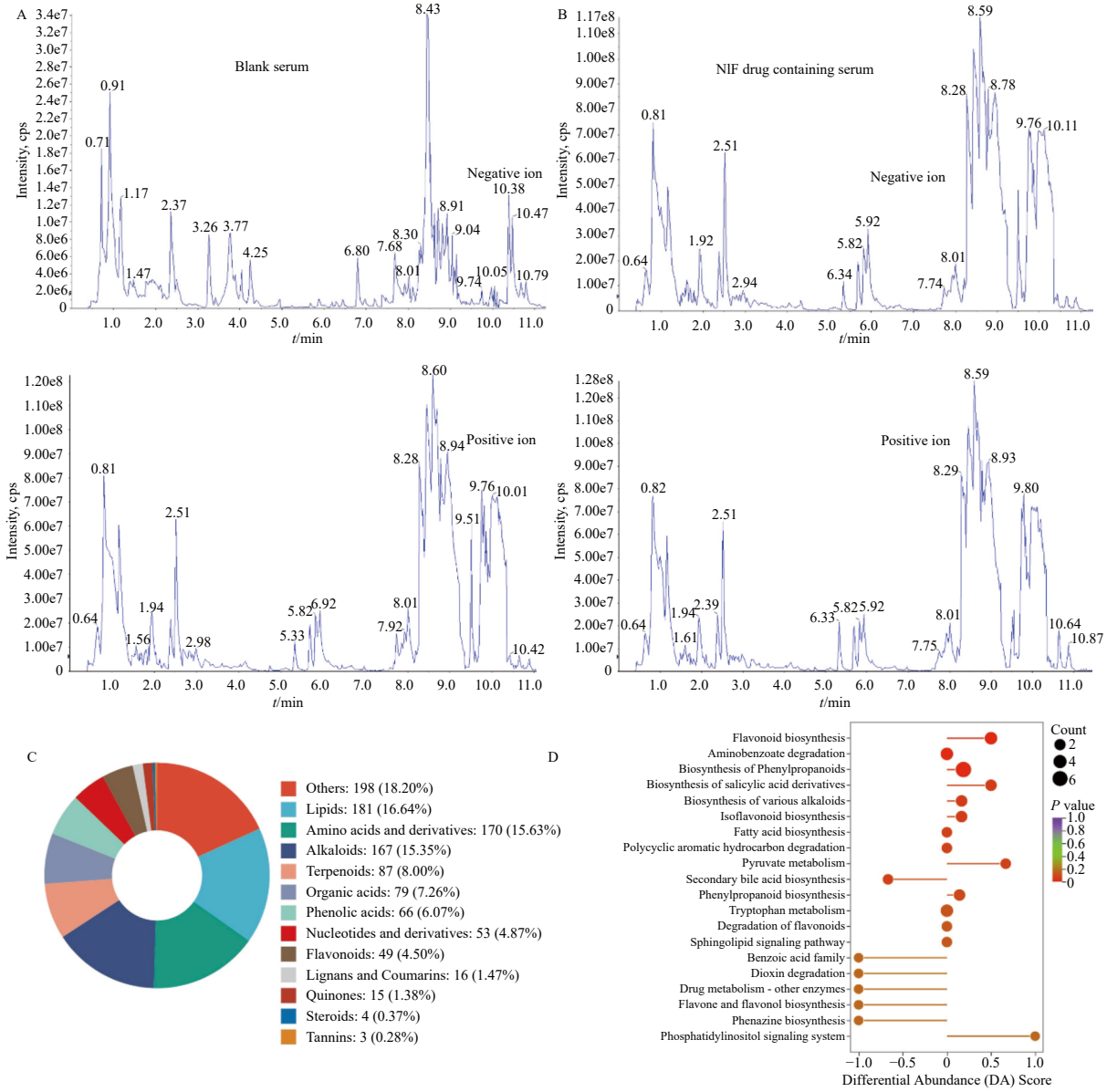

Fig. 1 Total ion flow map for natural product characterization in blank serum and N1F drug-containing serum samples. (A) Total ion flow map for natural product characterization in blank serum. (B) Total ion flow map for natural product identification in N1F drug-containing serum. (C) The composition of different categories of compounds in the serum. (D) KEGG pathway enrichment analysis of the target of differential components between blank and N1F drug-containing serum.

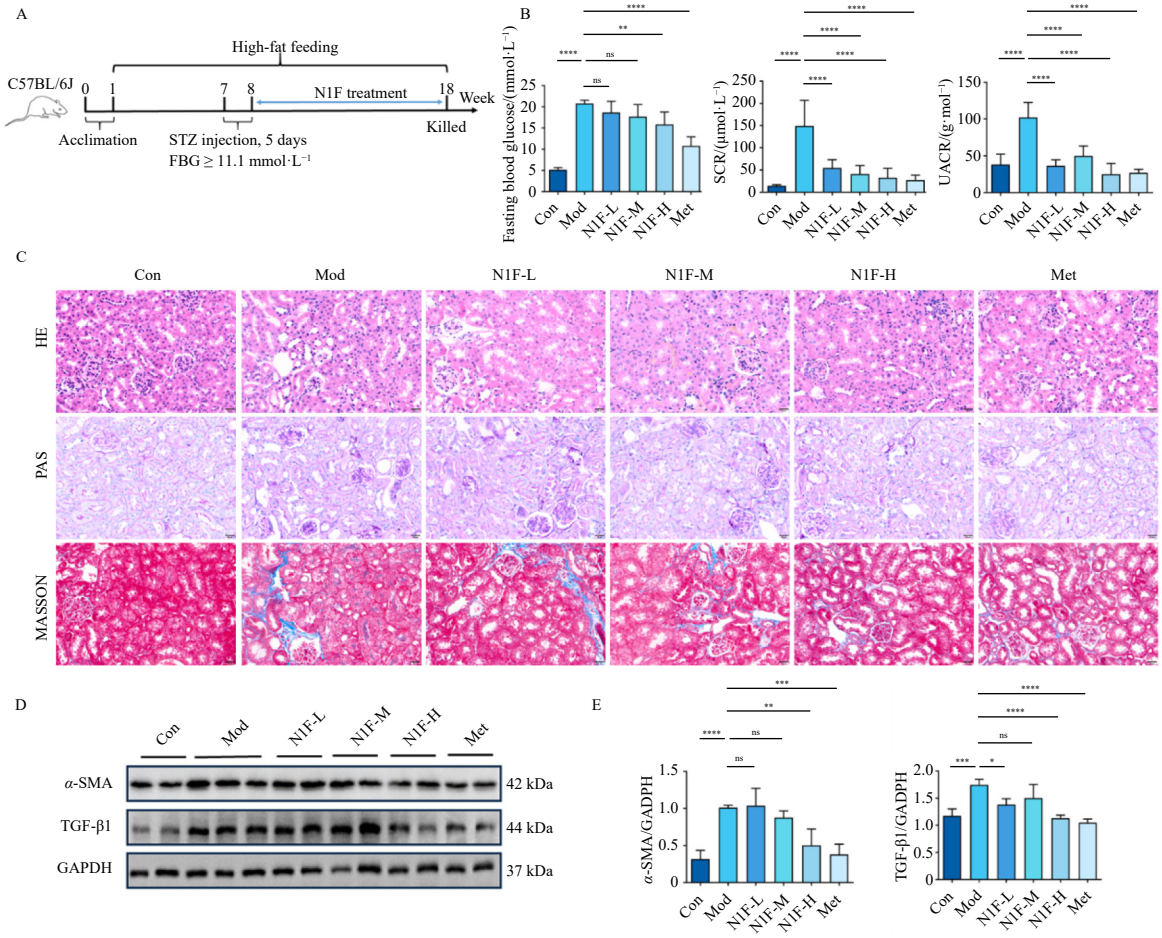

Fig. 2 Kidney dysfunction and renal injury ameliorated by NIF in T2DM mice. (A) Time course of N1F administration and sample collection. (B) Levels of fasting blood glucose, SCR in the serum, and UACR in the urine (n = 6). (C) Representative images of renal tissues stained with H&E, PAS, and Masson trichrome (scale bar = 50 μm). (D and E) Western blotting bands and quantitative analysis of α-SMA and TGF-β1 expression in kidney tissues of T2DM mice (n = 4). Data are presented as means ± SD. $^{*}P < 0.05$, $^{**}P < 0.01$, $^{***}P < 0.001$, and $^{****}P < 0.0001$; *ns*: not significant.

2C). Loading plots identified key contributing metabolites: in kidney tissues, these included lactate, succinate, taurine, TMAO, acetate, tyrosine, glycine, and inosine (Fig. 3D); in urine, TMA, TMAO, 2-PPA, creatine, and formate were prominent (Supporting Fig. 1D); in feces, cholate, valine, butyrate, alanine, acetate, choline, and tyrosine exhibited significant differences (Supporting Fig. 2D). Notably, T2DM mice displayed elevated levels of TMAO and energy metabolism–related metabolites (lactate and fumarate) in kidney tissues, which were reduced following N1F treatment (Fig. 3F). Conversely, the decreased succinate levels observed in the Mod group were restored by N1F administration. Renal TMA levels were significantly lower in T2DM mice than in controls but were normalized by N1F treatment (Fig. 3F). N1F suppressed plasma TMAO and TMA levels (Fig. 3E) and reduced urinary TMAO concentrations (Supporting Fig. 1E). Correlation analysis revealed significant positive associations between kidney injury markers (SCR and UACR) and several metabolites, including kidney TMAO, lactate, fumarate, serum TMAO, serum TMA, and urine TMAO. In contrast, negative correlations were observed between kidney TMA and succinate levels (Fig. 3G and Supporting Fig. 2F). Collectively, these data suggest that N1F ameliorates renal injury in T2DM mice by modulating dysregulated TMAO and energy metabolism pathways.

Compared to the Con group, T2DM mice exhibited significantly reduced levels of gut microbiota–derived metabolites, including isobutyrate and 2-PPA in urine, and acetate and butyrate in feces. Notably, N1F treatment reversed these reductions. In contrast, urine formate, another gut microbiota, associated metabolite, was markedly elevated in T2DM mice and substantially reduced after N1F administration (Supporting Figs. 1E and 2E). Correlation analysis revealed significant negative associations between kidney injury markers (SCR and UACR), kidney TMAO, serum TMAO, and levels of urine isobutyrate, urine 2-PPA, fecal acetate, and fecal butyrate. Conversely, urine formate showed a significant positive correlation with these parameters (Supporting Fig. 2F). These findings suggest that N1F may exert renoprotective effects by regulating gut microbiota–derived metabolites.

3.4. N1F inhibited renal pyroptosis induced by TMAO in vivo and in vitro

To elucidate the mechanism by which N1F improves renal injury, RNA sequencing was performed on kidney tissues. Principal component analysis (PCA) revealed distinct clustering among the Con, Mod, and N1F-H groups, with the N1F-H group clustering closer to the Con group, suggesting normalization of the transcriptomic profile upon N1F treatment (Fig. 4A). KEGG enrichment analysis of differentially expressed genes (DEGs) indicated that the NOD-like receptor signaling pathway was the most significantly enriched among the top 20 pathways (Fig. 4B). Moreover, 12 DEGs involved in this pathway were identified (Fig. 4C). The NLRP3 inflammasome, a critical mediator of immune-inflammatory responses, plays a key role in non-infectious inflammatory diseases and is increasingly implicated in DN pathogenesis [39, 40]. NLRP3 inflammasome activation promotes renal pyroptosis and accelerates DN progression through casp1 activation, GSDMD-mediated membrane pore formation, and release of IL-1β and IL-18 [27, 41]. Immunohistochemical analysis demonstrated that N1F reduced the expression of NLRP3 and GSDMD in T2DM mice (Figs. 4D and 4E). Western blotting results confirmed that N1F

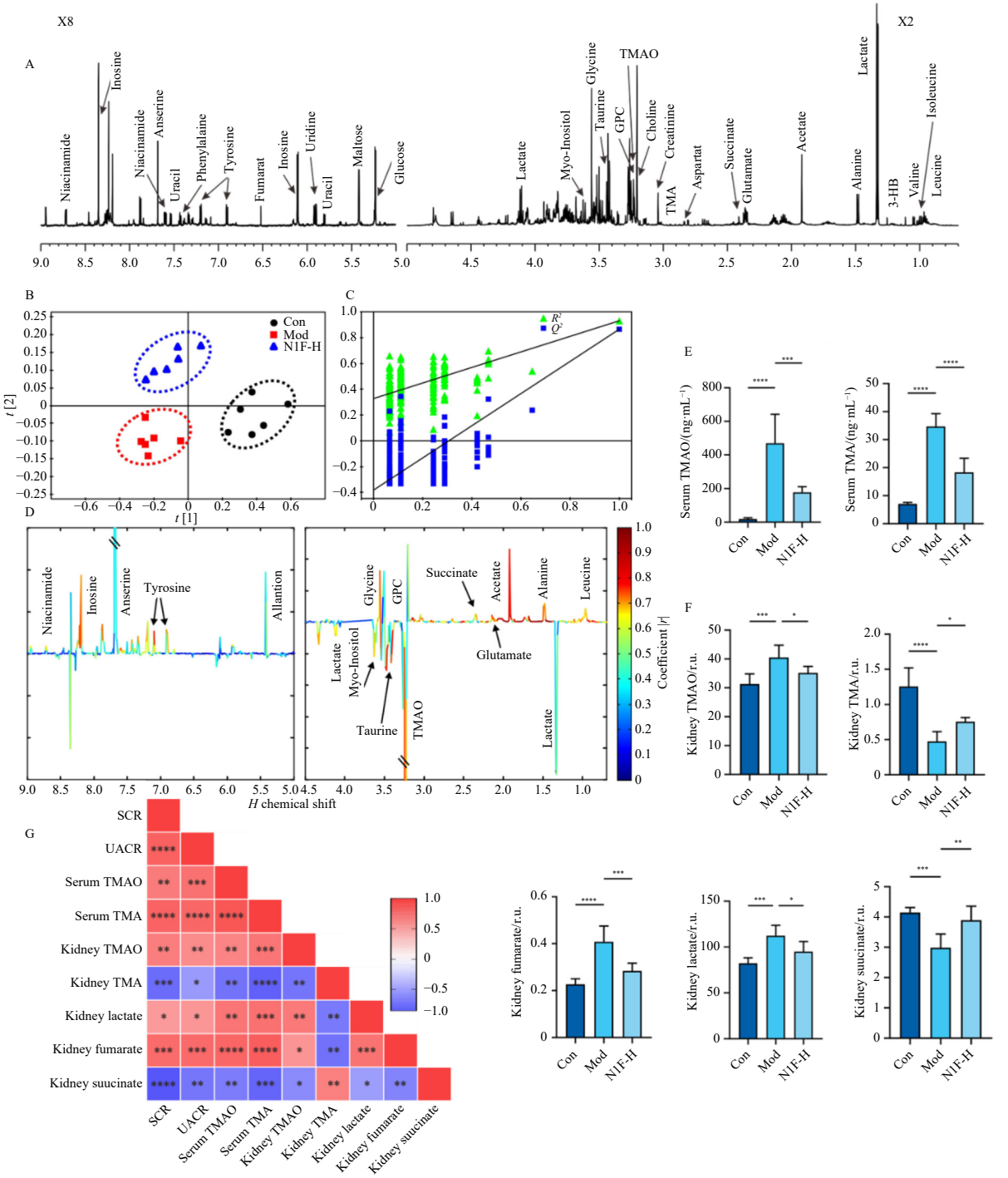

Fig. 3 Abnormal TMAO and energy metabolism were regulated in T2DM mice administered high-dose N1F. (A) Typical 600 MHz ^{1}H NMR spectra of the kidney in mice. (B) PLS-DA score plot of kidney in mice (R^2_X = 0.535, R^2_Y = 0.879, Q^2 = 0.586, P < 0.001). (C) Permutation test (200 cycles, R^2 = 0.787, Q^2 = 0.758). (D) Coefficient-coded loading plot. (E) The levels of TMA and TMAO in serum (n = 6). (F) Metabolic changes in the kidney, including TMAO, TMA, fumarate, lactate, and succinate levels (n = 6). (G) Correlation analysis of kidney and serum metabolic changes with the kidney injury-related index (n = 6). Data are shown as means ± SD. $^{*}P$ < 0.05, $^{**}P$ < 0.01, $^{***}P$ < 0.001, and $^{****}P$ < 0.0001.

significantly decreased protein levels of NLRP3, cleaved-IL-1β, IL-18, cleaved-casp1, and N-GSDMD in kidney tissues (Figs. 4F and 4G). Serum levels of IL-1β and IL-18 were also significantly reduced following N1F treatment (Fig. 4H). These findings indicate that N1F suppresses NLRP3 inflammasome activation, thereby inhibiting renal pyroptosis.

Given that elevated TMAO levels can induce renal pyroptosis and contribute to DN pathogenesis [41, 42], and that N1F regulates TMAO metabolism, we investigated the protective effect of N1F against TMAO-induced pyroptosis *in vitro* using MES-13 cells. Cells were exposed to HG or TMAO to simulate the diabetic microenvironment. HG stimulation increased levels of mROS, TGF-β, N-GSDMD, IL-1β, and IL-18 (Figs. 4I–4N). Exposure to TMAO or HG + TMAO further elevated the expression of mROS, α-SMA, TGF-β, NLRP3, N-GSDMD, cleaved-casp1, IL-1β, and IL-18, indicating synergistic effects of glucose and TMAO on pyroptosis and fibrosis. Treatment with N1F-containing serum significantly reversed the HG + TMAO–induced increases in these markers (Figs. 4I–4N). Notably, mROS levels were significantly higher under HG + TMAO than in the HG-only group, supporting a role for TMAO in promoting mitochondrial oxidative stress (Figs. 4I and 4J). Additionally, fibrosis-related proteins (α-SMA and TGF-β1) and pyroptosis-related proteins (NLRP3, N-GSDMD, cleaved-casp1, IL-1β, and IL-18) were significantly upregulated in the

HG + TMAO group compared to the HG group, and were effectively suppressed by N1F treatment (Figs. 4K–4N). Collectively, these results support a role for TMAO in inducing pyroptosis and demonstrate that N1F intervenes in this process, in addition to its regulation of TMAO metabolism.

3.5. Potential mechanism of N1F in pyroptosis: mROS-NLRP3 axis intervention

Accumulating evidence indicates that excessive mROS generated by damaged mitochondria can activate the NLRP3 inflammasome and promote pyroptosis [13, 43]. To examine the role of mROS in HG + TMAO–induced pyroptosis, MitoTEMPO, a specific mitochondrial anti-oxidant, was used. MitoTEMPO treatment significantly suppressed the expression of fibrosis-associated proteins (α-SMA, TGF-β1) and pyroptosis-associated markers (NLRP3, N-GSDMD, cleaved-casp1, IL-1β, and IL-18) in MES-13 cells exposed to HG + TMAO (Figs. 5A–5E). These effects were comparable to those of N1F-containing serum, indicating that mROS inhibition effectively mitigates pyroptosis. Moreover, combined treatment with MitoTEMPO and N1F resulted in a greater reduction in IL-1β and IL-18 levels than either treatment alone (Fig. 5E). Fluorescence probe staining was used to assess mROS levels. HG + TMAO stimulation caused a substantial increase in mROS, likely due to mitochondrial damage. Both MitoTEMPO and N1F treatments significantly reduced mROS levels, and their combination exhibited an additive effect (Figs. 5A and 5B). These findings suggest that N1F exerts anti-oxidant activity by scavenging mROS, thereby mitigating downstream pyroptotic signaling.

To assess the involvement of the NLRP3 inflammasome in HG + TMAO-induced pyroptosis, MES-13 cells were treated with MCC950, a selective NLRP3 inhibitor. MCC950 significantly downregulated the expression of fibrosis- and pyroptosis-associated proteins (Figs. 5F–5H). Co-treatment with N1F further enhanced these suppressive effects. Overall, these results suggest that N1F mitigates pyroptosis by reducing TMAO levels, inhibiting mROS accumulation, and suppressing NLRP3 inflammasome activation, thereby protecting against diabetic renal injury.

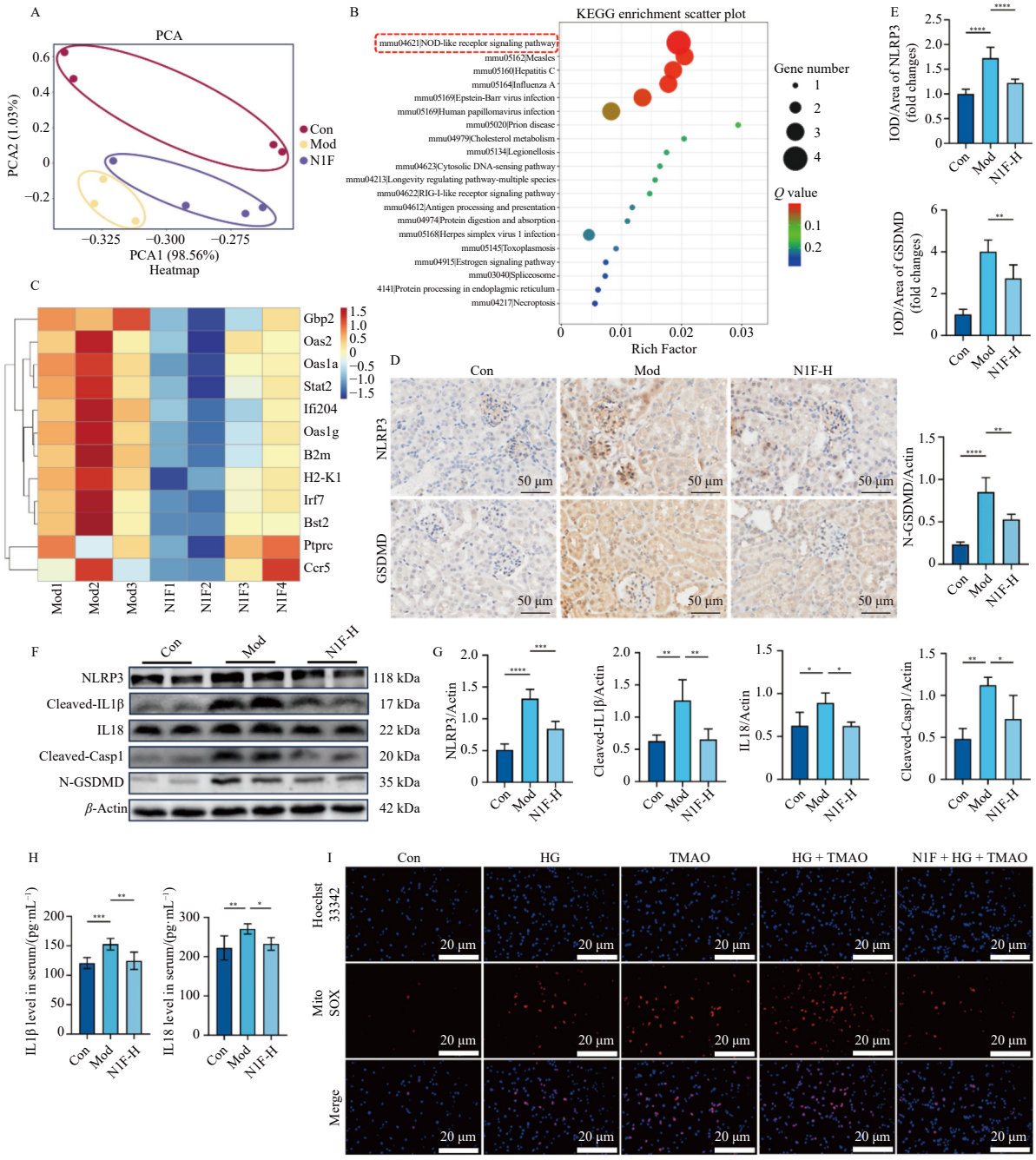

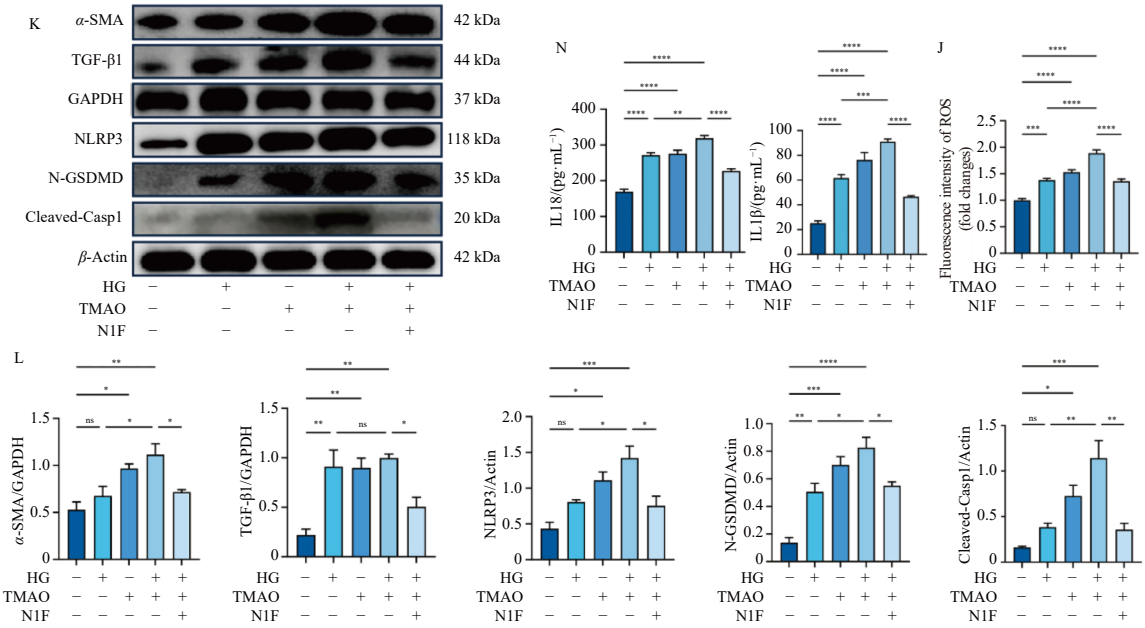

Fig. 4 N1F attenuates TMAO-induced renal pyroptosis *in vivo* and *in vitro*. (A) PCA of the Con, Mod, and N1F high-dose groups based on differential gene expression. (B) KEGG analysis of differential genes between the Mod and N1F high-dose groups. (C) Heatmap of DEGs related to NOD-like receptor signaling pathway in Mod and N1F high-dose groups. (D and E) Immunohistochemical images and statistical assessment of NLRP3 and GSDMD in the kidney sections of mice (n = 6, scale bar = 50 μm). (F and G) Typical Western blotting bands and quantitative assessment of pyroptosis-related proteins in renal tissues of mice (n = 4). (H) The levels of IL1β and IL18 in the serum (n = 6). (I and J) Images and statistical assessment of mROS level in MES-13 cells (n = 6, scale bar=20 μm). (K and L) Western blotting bands and quantitative analysis of α-SMA, TGF-β1, and pyroptosis-related proteins in MES-13 cells (n = 3). (M) The levels of IL1β and IL18 in the culture medium of MES-13 cells (n = 6). Data are shown as means ± SD. $^{*}P < 0.05$, $^{**}P < 0.01$, $^{***}P < 0.001$, and $^{****}P < 0.0001$; *ns*: not significant.

3.6. N1F attenuated mitochondrial dysfunction in vivo and in vitro

Hyperglycemia-induced oxidative stress promotes mitochondrial damage and pyroptosis through excessive ROS production [44, 45]. TEM revealed mitochondrial structural abnormalities in the kidneys of T2DM mice, including disrupted membranes, loss of cristae, and matrix dilution (Fig. 6A). N1F treatment restored mitochondrial integrity. In the T2DM model, mitochondrial dynamics were impaired: expression of the Mfn2 was significantly downregulated, while the fission protein Fis1 was upregulated (Supporting Fig. 3 and Figs. 6C and 6D), indicating excessive mitochondrial fragmentation. Furthermore, mRNA and protein levels of mitochondrial respiratory chain components—SDHB, UQCRC2, and ATP5A1—were significantly reduced (Supporting Fig. 3 and Figs. 6C and 6D), along with decreased renal ATP levels (Fig. 6B), indicating severe impairment of mitochondrial energy metabolism. N1F administration reversed these alterations, enhancing mitochondrial biogenesis, restoring respiratory function, and normalizing mitochondrial dynamics.

To validate the protective effect of N1F on mitochondria *via* mROS modulation, MES-13 cells were subjected to HG and TMAO stimulation. JC-1 staining showed that N1F-containing serum restored the mitochondrial membrane potential disrupted by HG + TMAO, similar to the effect of the mitochondrial-targeted anti-oxidant MitoTEMPO (Figs. 6E and 6F). Both N1F and MitoTEMPO treatments increased expression of Mfn2, SDHB, UQCRC2, and ATP5A1, elevated cellular ATP levels, and suppressed Fis1 expression (Figs. 6G, 6H, and 6M). Functional analysis using Seahorse XF96 assays revealed that HG + TMAO exposure suppressed mitochondrial OXPHOS, as indicated by reduced OCR (Fig. 6I), and enhanced glycolysis, reflected by increased ECAR (Fig. 6K). Correspondingly, mitochondrial respiratory capacity was diminished (Fig. 6J), while glycolytic capacity was elevated (Fig. 6L), indicating a shift toward glycolytic metabolism and mitochondrial dysfunction. However, both MitoTEMPO and N1F-containing serum treatment significantly reversed these impairments. Combined treatment with MitoTEMPO and N1F further improved mitochondrial function (Figs. 6E–6M). These results suggest that N1F alleviates ROS-dependent mitochondrial dysfunction and protects renal function.

3.7. N1F inhibited TMAO-related metabolite production with alteration of the gut microbiome

TMAO, a key mediator in the gut-kidney axis, is produced by gut microbial enzymes and hepatic FMO3 [46, 47]. N1F significantly

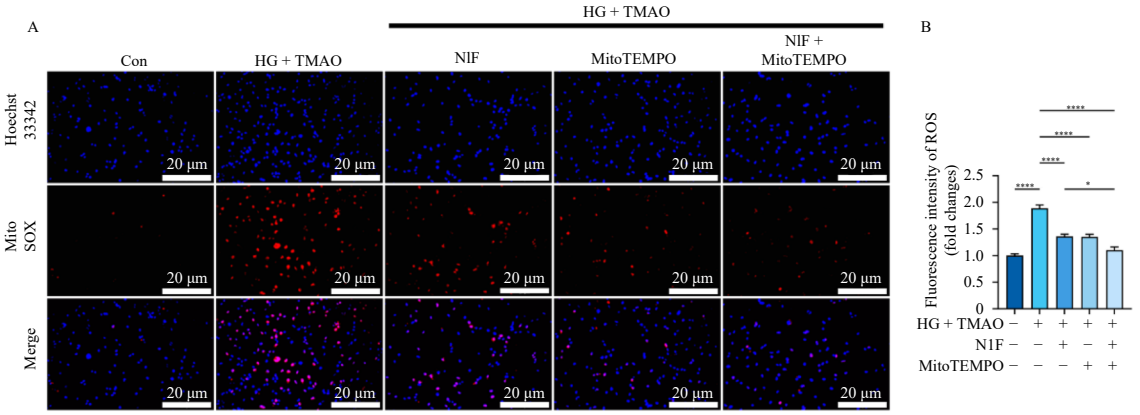

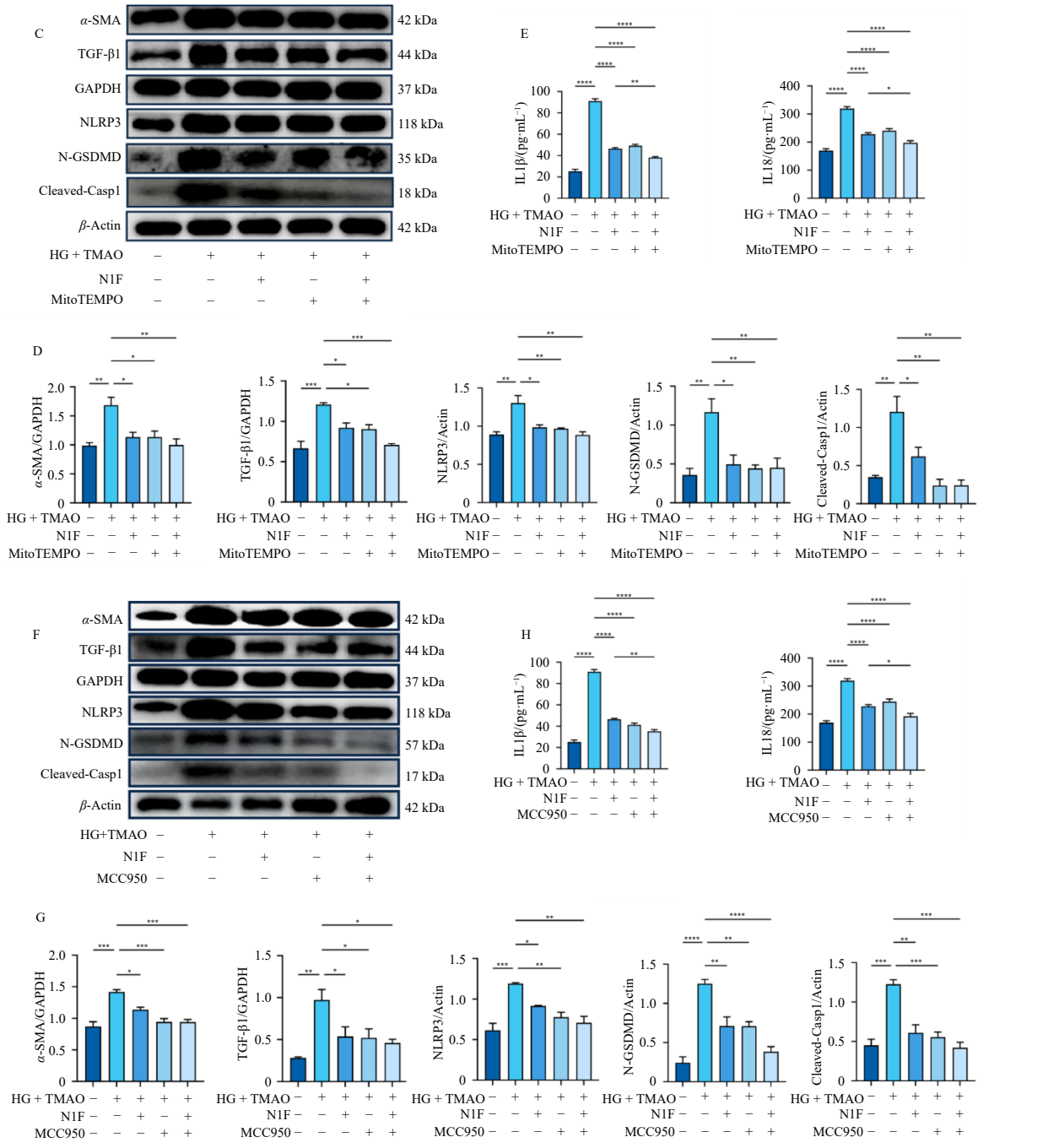

Fig. 5 N1F ameliorates pyroptosis by suppressing the mROS-NLRP3 axis in MES-13 cells. (A and B) Images and statistical assessment of mROS level in MES-13 cells (n = 6, scale bar = 20 μm). (C and D) Typical Western blotting bands and quantitative analysis of α-SMA, TGF-β1, and pyroptosis-related proteins in MES-13 cells (n = 3). (E) The levels of IL1β and IL18 in MES-13 cell medium (n = 6). (F and G) Western blotting bands and quantitative analysis of α-SMA, TGF-β1, and pyroptosis-related proteins in MES-13 cells (n = 3). (H) Levels of IL1β and IL18 in the culture medium of MES-13 cells (n = 6). Data are presented as means ± SD. $^{*}P < 0.05$, $^{**}P < 0.01$, $^{***}P < 0.001$, and $^{****}P < 0.0001$.

reduces TMAO levels in plasma, kidney, and urine, and modulates several gut microbiota-derived metabolites. To determine whether the TMAO-lowering effect of N1F is mediated *via* gut microbiota modulation, 16S rRNA gene sequencing was performed to evaluate microbial composition and its potential role in TMAO metabolism following N1F treatment. Alpha diversity indices (Chao1, Shannon, Simpson, and observed species) were significantly increased in the N1F high-dose group compared to T2DM mice, indicating enhanced microbial richness and evenness (Fig. 7A). Principal coordinate analysis (PCoA) revealed distinct clustering among control, model, and N1F-treated groups, indicating significant differences in microbial community structure (Fig. 7B). Taxonomic profiling at the phylum level showed that *Firmicutes* and *Bacteroidota* were elevated in T2DM mice, while *Actinobacteria* were reduced. N1F treatment partially restored the balance of these phyla (Fig. 7C). Linear discriminant analysis effect size (LEfSe) identified 50 bacterial genera with significantly altered abundance across the three groups (Fig. 7E). Among them, eight genera—*Alistipes_A*, *Tidjanibacter*, *Prevotella*, *Acetatifactor*, *Limosilactobacillus*, *Clostridium_T*, *Faecalibaculum*, and *Lawsonibacter*—were enriched in T2DM mice but significantly reduced following N1F intervention (Fig. 7D). In contrast, N1F significantly increased beneficial genera such as *Bifidobacterium*, *Akkermansia*, *Adlercreutzia*, *Dubosiella*, and *Duncaniella* (Fig. 7D). Importantly, *Clostridium_T*, *Prevotella*, and *Alistipes_A* have been associated with the production of TMA, a precursor of TMAO [48–50].

Although hepatic FMO3 expression was elevated in T2DM mice, N1F did not significantly alter its expression (Supporting Fig. 4), suggesting that the TMAO-lowering effect is primarily mediated by gut microbiota. Overall, these results indicate that N1F modulates gut microbiota composition, particularly by reducing the abundance of TMA-producing bacteria, thereby contributing to lower systemic TMAO levels in T2DM mice.

4. Discussion

In China, diabetic kidney disease has surpassed glomerulonephritis as the leading cause of chronic kidney disease (CKD). Despite therapeutic advances, current treatments for DN remain suboptimal, with response rates between 20% and 30%, and frequent adverse effects such as hyperkalemia [51]. These limitations underscore the need for safer and more effective therapeutic strategies. TCM has gained recognition as a complementary or alternative approach for DN due to its multi-component, multi-target mechanisms and favorable safety profile. Formulations such as Tangshen Formula (TSF) modulate gut microbiota and reduce uremic toxin production in DN models [52]. N1F, derived from classical prescriptions, demonstrates promising clinical efficacy in DN treatment. However, its underlying molecular mechanisms were previously undefined. This study reveals that N1F ameliorates mitochondrial dysfunction and pyroptosis in DN through the TMAO-mROS-NLRP3 signaling axis, providing novel mechanistic insights that support the future clinical application of N1F. Our conclusions are supported by three key findings: (i) N1F significantly improves UACR, renal function, and histopathological damage in T2DM mice; (ii) N1F modulates TMAO and energy metabolism by altering gut microbiota composition and suppressing TMAO-related metabolite production; and (iii) N1F alleviates mROS-dependent mitochondrial dysfunction and TMAO-induced pyroptosis.

Metabolic dysregulation plays a central role in DN pathogenesis. Persistent hyperglycemia leads to excessive intracellular glucose accumulation, disrupting the metabolism of glucose, lipids, proteins, and methylamines [53]. In DN, renal metabolic repro-

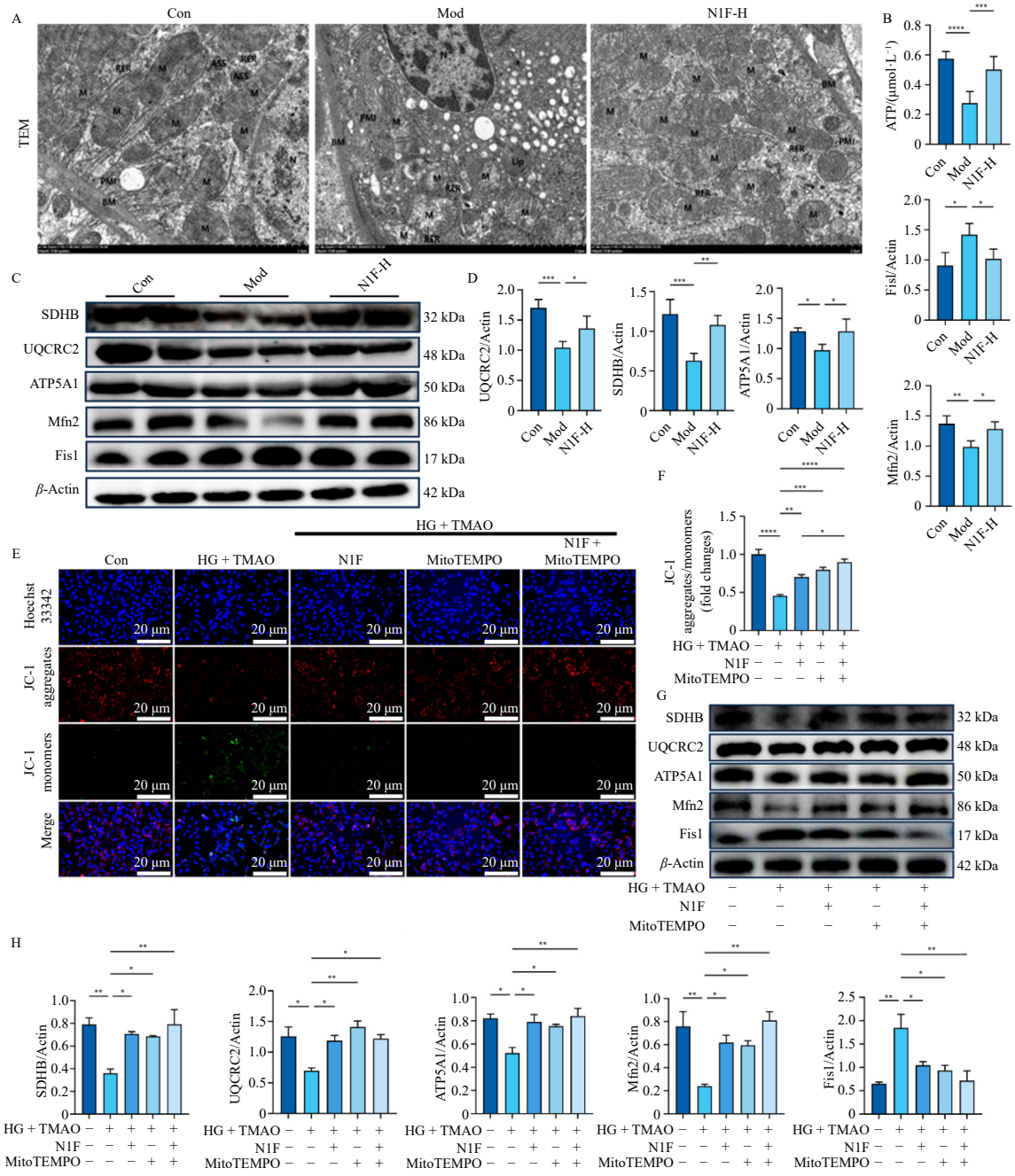

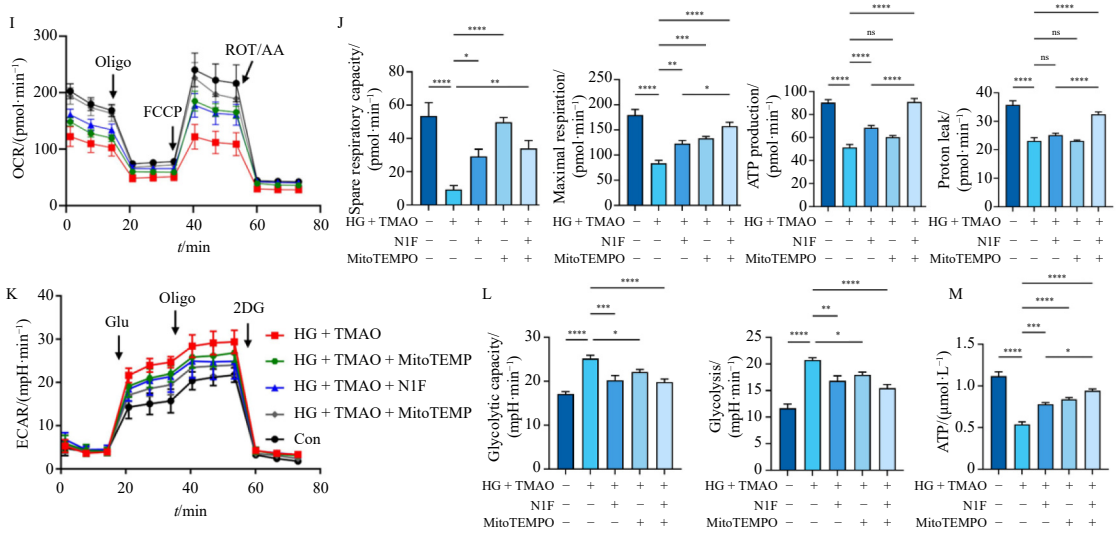

Fig. 6 N1F eliminates mitochondrial dysfunction *in vivo* and *in vitro*. (A) Representative TEM images of renal tissues (scale bar = 2 μm). (B) The level of ATP in kidney tissues (n = 6). (C and D) Western blotting bands and quantitative assessment of SDHB, UQCRC2, ATP5A1, Mfn2, and Fis1 expression in kidney tissues of T2DM mice (n = 4). (E and F) Typical images and statistical assessment of mitochondrial membrane potential level in MES-13 cells (n = 6, scale bar = 20 μm). (G and H) Western blotting bands and quantitative assessment of SDHB, UQCRC2, ATP5A1, Mfn2, and Fis1 expression in MES-13 cells (n = 3). (I) Profile of seahorse oxygen consumption rate (OCR) with Cell Mito Stress Test. (J) Statistical analyses of spare respiratory capacity, maximal respiration, ATP production, and proton leak in OCR (n = 6). (K) Profile of the seahorse extracellular acidification rate (ECAR) with the Glycolysis Stress Test. (L) Statistical analyses of glycolysis and glycolytic capacity in ECAR (n = 6). (M) The level of ATP in MES-13 cells (n = 6). Data are shown as means ± SD. $^{*}P < 0.05$, $^{**}P < 0.01$, $^{***}P < 0.001$, and $^{****}P < 0.0001$; *ns*: not significant.

gramming is characterized by increased glycolysis and reduced TCA cycle activity, resulting in the accumulation of metabolic intermediates and subsequent renal injury [54]. Elevated lactate levels have been shown to exacerbate renal dysfunction and fibrosis [55]. TCM has increasingly attracted attention for its ability to modulate metabolic disorders in DN. Emodin, a systemically absorbed component of N1F, regulates gene expression, inhibits podocyte epithelial-to-mesenchymal transition (EMT), corrects glucose and lipid metabolism abnormalities, and protects renal cells [56]. In this study, T2DM mice exhibited significant elevations in blood glucose, SCR, and UACR. Histological analyses using H&E, PAS, and Masson's trichrome staining confirmed structural renal injury. TMAO and energy metabolism were disrupted in T2DM mice. Notably, N1F treatment attenuated these diabetes-induced abnormalities, significantly improving kidney function and reducing renal injury. Metabolomic assessment indicated that N1F modulated TMAO and energy metabolism, thereby mitigating diabetes-associated renal damage.

Gut-derived uremic toxins have recently drawn substantial scientific interest, with TMAO—a gut microbiota-dependent metabolite—linked to both diabetes and cardiovascular diseases [12]. In this study, metabolomic analysis revealed that N1F significantly reversed elevated TMAO levels in the kidneys, serum, and urine of T2DM mice. TMAO acts as an independent risk factor that promotes disease progression by inducing pyroptosis. Its accumulation disrupts mitochondrial structure and function, enhances mROS production, and activates the NLRP3 inflammasome. This activation triggers casp1 and GSDMD, leading to the release of pro-inflammatory cytokines such as IL-1β and IL-18, ultimately causing pyroptotic cell death [57]. Transcriptomic analysis suggested that N1F may limit renal injury in T2DM mice by regulating the NOD-like receptor signaling pathway. Rhein, another systemically absorbed constituent of N1F, exerts anti-inflammatory effects by inhibiting NF-κB activation, thereby preventing NLRP3 inflammasome assembly and suppressing casp1 activity, which reduces IL-1β levels [58]. Baicalin exhibits anti-pyroptotic properties by promoting autophagic degradation of p30/GSDMD and disrupting ASC oligomerization, thus inhibiting NLRP3 inflammasome activation [59]. Therefore, we investigated the potential inhibitory effect of N1F on TMAO-induced pyroptosis. Our data showed that N1F treatment significantly reduced levels of NLRP3, cleaved-IL-1β, IL-18, cleaved-casp1, and N-GSDMD *in vivo* and *in vitro*. Treatment of MES-13 cells with HG and TMAO markedly increased pyroptosis markers compared to HG alone, whereas N1F effectively attenuated their expression. These results indicate that N1F mitigates TMAO-induced pyroptosis, contributing to delayed DN progression.

Prior studies have demonstrated that TMAO markedly increases mROS production, thereby activating the NLRP3 inflammasome. To elucidate the mechanism by which N1F suppresses TMAO-induced pyroptosis, we examined the TMAO-mROS-NLRP3 signaling axis. mROS levels were significantly elevated in MES-13 cells treated with HG and TMAO compared to HG alone. However, treatment with the mitochondria-targeted anti-oxidant MitoTEMPO or N1F-containing serum substantially reduced mROS accumulation. Combined treatment with MitoTEMPO and N1F further enhanced this reduction. Moreover, MitoTEMPO suppressed HG + TMAO-induced pyroptosis and renal fibrosis. MCC950, a selective NLRP3 inflammasome inhibitor, significantly reduced the expression of fibrosis- and pyroptosis-related proteins, and its combination with N1F amplified these protective effects. Collectively, these findings demonstrate that N1F alleviates pyroptosis in DN by modulating the TMAO-mROS-NLRP3 pathway.

Mitochondrial dysfunction is a critical contributor to DN pathogenesis. Beyond serving as the primary source of cellular energy, mitochondria regulate redox homeostasis, fatty acid oxidation, calcium signaling, and apoptosis [60]. In DN patients and animal models, mitochondrial abnormalities include impaired mitophagy, reduced OXPHOS efficiency, and diminished ATP synthesis. These defects contribute to tubular and glomerular injury and exacerbate disease progression through oxidative stress, inflammation, and pyroptosis [61]. Evidence underscores the pathogenic roles of excessive mROS and metabolic imbalance in DN [62]. This study demonstrated that N1F scavenges mROS and attenuates pyroptosis. To explore this protective mechanism, we evaluated the effects of N1F on diabetes-induced mitochondrial dysfunction. Baicalin, a major systemically absorbed component of N1F, enhances mitochondrial function and dynamics during *Staphylococcus aureus* infection [63] and ameliorates mitochondrial damage *via* the Pdk-Pdc signaling axis [64]. Mitochondrial fission involves loss of membrane potential and mitochondrial DNA fragmenta-

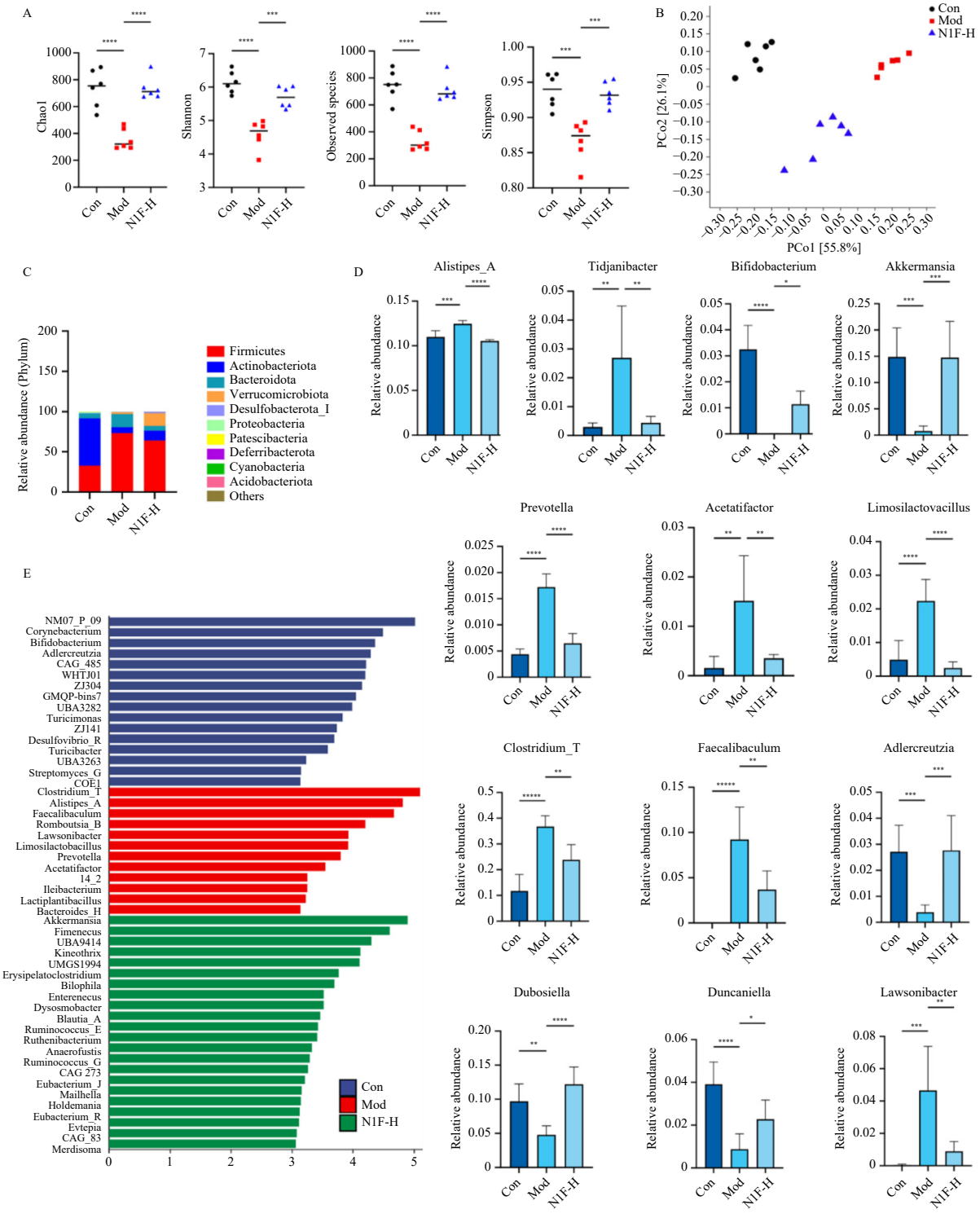

Fig. 7 16S rRNA sequencing reveals altered microbiota composition following N1F treatment. (A) Alpha diversity, including Chao1, Shannon, Observed species, and Simpson index ($n = 6$). (B) The beta diversity on OUT levels of PCoA analysis. (C) Effects of N1F-H on gut microbiome modulation at the phylum levels. (D) Effects of N1F-H on fourteen gut microbiome groups ($n = 6$). (E) Analysis of taxonomic abundances using LEfSe. Histogram of LDA scores to identify differentially abundant bacterial genera (LDA score ≥ 3.0, Kruskal–Wallis = 0.05, Wilcoxon = 0.05, $n = 6$). Data are shown as means ± SD. $^{*}P < 0.05$, $^{**}P < 0.01$, $^{***}P < 0.001$, and $^{****}P < 0.0001$.

tion, whereas fusion is a more complex process that helps mitigate damage and prevents cell death [65]. We found that N1F significantly improved mitochondrial ultrastructure in the renal tissues of T2DM mice and restored mitochondrial dynamics by downregulating Fis1 and upregulating Mfn2 *in vivo* and *in vitro*. N1F also reversed the abnormal downregulation of mitochondrial respiratory chain proteins SDHB, UQCRC2, and ATP5A1 and restored ATP levels. Mitochondrial membranes play a crucial role in maintaining organelle stability [66]. N1F alleviated mitochondrial dysfunction, as evidenced by the restoration of mitochondrial membrane potential in HG + TMAO-treated MES-13 cells. Mitochondrial OXPHOS and glycolysis are two essential pathways governing mitochondrial function and cellular energy balance [12]. N1F normalized the OCR and ECAR, indicating enhanced OXPHOS and reduced glycolytic dependence. Together, these results suggest that N1F improves mitochondrial energy metabolism by promoting OXPHOS and ATP production while decreasing reliance on glycolysis. These findings align with our metabolomics data, which show that N1F modulates energy metabolism in T2DM mice.

Under diabetic conditions, hyperglycemia induces mitochon-

drial dysfunction characterized by excessive mROS generation, loss of mitochondrial membrane potential, and structural damage, impairing energy metabolism and exacerbating tissue injury [67]. To determine whether N1F ameliorates mitochondrial dysfunction *via* mROS scavenging, we used MitoTEMPO. MitoTEMPO restored mitochondrial membrane potential, corrected imbalances in mitochondrial dynamics, and normalized the expression of respiratory chain proteins in HG + TMAO-treated MES-13 cells. Seahorse metabolic flux analysis revealed that MitoTEMPO increased OXPHOS activity and ATP production while reducing glycolytic dependence. Combined treatment with MitoTEMPO and N1F resulted in more pronounced improvements in membrane potential and ATP generation. Thus, N1F mitigates HG + TMAO-induced mitochondrial dysfunction and energy metabolic disturbances by scavenging mROS.

Gut dysbiosis is a major driver of DN development and progression. TMAO production depends on hepatic FMO3-mediated metabolism and is strongly influenced by gut microbiota composition. In this study, metabolomic profiling of urine and feces revealed that N1F modulates gut microbiota-associated metabolites, suggesting a potential link between N1F and microbial regulation. Therefore, we characterized gut microbiota structure in T2DM mice, assessed the regulatory effects of N1F, and determined whether N1F modulates TMAO levels through gut microbiota modulation. N1F treatment significantly enhanced the diversity and richness of gut microbiota in T2DM mice. Taxonomic analysis showed that N1F increased the abundance of *Firmicutes* and *Bacteroidota* while reducing *Actinobacteria*. These three phyla constitute dominant members of the gut microbiota, and the *Firmicutes*/*Bacteroidota* (F/B) ratio serves as a key indicator of microbial homeostasis. Alterations in this ratio are associated with lipid metabolism disorders and bile acid dysregulation, contributing to obesity and diabetes [68, 69]. Quantitative analysis identified 13 genera significantly reduced by N1F: *Alistipes A*, *Tidjanibacter*, *Prevotella*, *Acetatifactor*, *Limosilactobacillus*, *Clostridium_T*, *Faecalibaculum*, *Lawsonibacter*, *Bifidobacterium*, *Akkermansia*, *Adlercreutzia*, *Dubosiella*, and *Duncaniella*. These taxa play vital roles in host metabolic homeostasis.

Alistipes_A regulates obesity-related metabolic parameters and is negatively correlated with lipid levels in diabetic patients [70]. As a TMA-producing bacterium, *Alistipes_A* is positively associated with TMAO production [48]. Li et al. reported that *Prevotella* harbors genomic features including *CutC* and *CutD* genes, enabling choline, L-carnitine, and betaine metabolism into TMA, thereby promoting TMAO accumulation and accelerating atherosclerosis [71]. The abundance of *Clostridium_T* in T2DM patients correlates positively with plasma glucose levels. Statin therapy reduces *Clostridium_T* abundance, influencing bile acid and glucose metabolism [72]. Notably, *Clostridium_T* also participates in choline-to-TMA conversion and is enriched in the gut microbiota of individuals with kidney disease [73]. *Faecalibaculum* correlates with blood urea nitrogen (BUN) levels in hyperuricemic rats and with metabolic disturbances during diabetes progression [74]. Zhang et al. reported that *Faecalibaculum* abundance was markedly increased in mice fed a high L-carnitine diet and closely linked to TMAO production [75]. Overall, N1F treatment ameliorates gut microbiota dysbiosis in T2DM mice. Our findings indicate increased abundance of bacteria involved in TMAO metabolism and enrichment of related pathways such as choline metabolism. Although hepatic FMO3 expression was elevated in T2DM mice relative to controls, this increase was not reversed by N1F treatment. Our study suggests that N1F alleviates diabetic kidney injury by reducing TMAO levels through modulation of gut microbial populations rather than hepatic FMO3 activity.

This study evaluates the therapeutic effects and underlying mechanisms of N1F in DN. N1F ameliorates renal injury by modulating TMAO and energy metabolism in T2DM mice. Specifically, N1F reduces the abundance of TMAO-producing bacteria, decreases TMAO synthesis, suppresses mROS overproduction, restores mitochondrial homeostasis and energy metabolism, and subsequently attenuates pyroptosis *in vivo* and *in vitro*. These findings demonstrate that N1F alleviates mitochondrial dysfunction and pyroptosis *via* the TMAO-mROS-NLRP3 axis, exerting a protective effect against DN (Fig. 8). This work provides robust evidence supporting the therapeutic potential of N1F as a novel strategy for DN treatment.

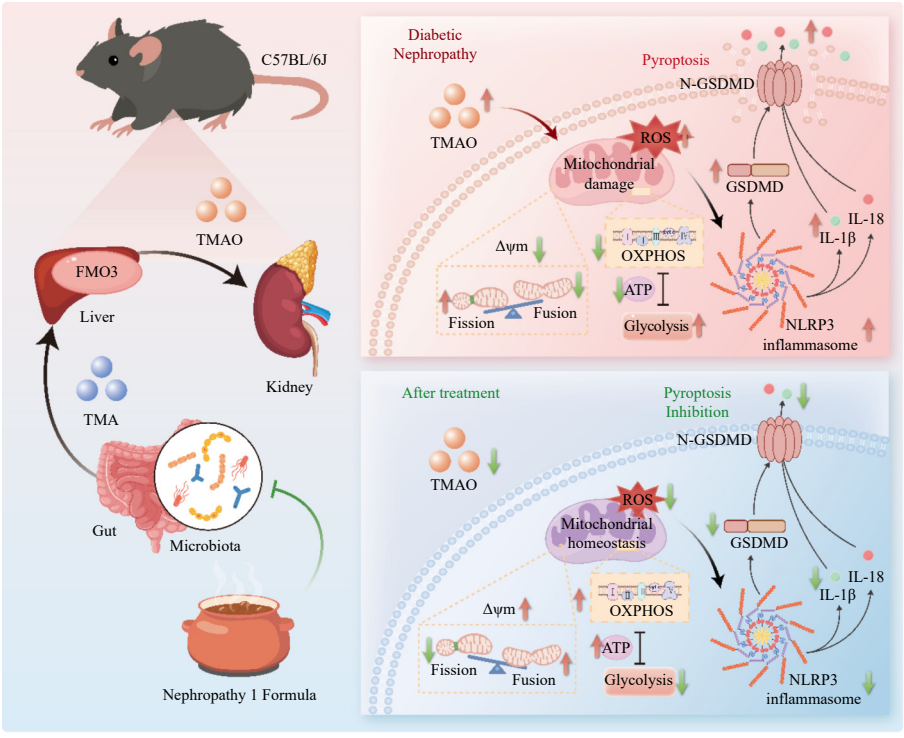

Fig. 8 Illustration of the molecular mechanism of N1F on DN.

Funding

This work was supported by the Science and Technology Department Research and Development Project of Zhejiang Province, China (No. 2022C03160) and the Traditional Chinese Medicine of Zhejiang Provincial Science and Technology Program Project (No. GZY-ZJ-KJ-24037).

Declaration of competing interest

The authors declare that they have no known competingfinancial interests or personal relationships that could haveappeared to influence the work reported in this paper.

References

1 Samsu N. Diabetic nephropathy: challenges in pathogenesis, diagnosis, and treatment. *Biomed Res Int*. 2021;2021:1497449. https://doi.org/10.1155/2021/1497449.
2 Qi MS, Hu XK, Zhu WJ, et al. Study on effects and relevant mechanisms of Mudan Granules on renal fibrosis in streptozotocin-induced diabetes rats. *Ren Fail*. 2024;46(1):2310733. https://doi.org/10.1080/0886022X.2024.2310733.
3 Mise K, Galvan DL, Danesh FR. Shaping up mitochondria in diabetic nephropathy. *Kidney360*. 2020;1(9):982-992. https://doi.org/10.34067/kid.0002352020.
4 Song L, Zhang W, Tang SY, et al. Natural products in traditional Chinese medicine: molecular mechanisms and therapeutic targets of renal fibrosis and state-of-the-art drug delivery systems. *Biomed Pharmacother*. 2024;170:116039. https://doi.org/10.1016/j.biopha.2023.116039.
5 Falkevall A, Mehlem A, Palombo I, et al. Reducing VEGF-B signaling ameliorates renal lipotoxicity and protects against diabetic kidney disease. *Cell Metab*. 2017;25(3):713-726. https://doi.org/10.1016/j.cmet.2017.01.004.
6 Wei TT, Shu Q, Ning J, et al. The protective effect of basic fibroblast growth factor on diabetic nephropathy through remodeling metabolic phenotype and suppressing oxidative stress in mice. *Front Pharmacol*. 2020;11:66. https://doi.org/10.3389/fphar.2020.00066.
7 Li MJ, Wang XF, Aa JY, et al. GC/TOFMS analysis of metabolites in serum and urine reveals metabolic perturbation of TCA cycle in db/db mice involved in diabetic nephropathy. *Am J Physiol Renal Physiol*. 2013;304(11):1317-1324. https://doi.org/10.1152/ajprenal.00536.2012.
8 Mosterd CM, Kanbay M, Van den Born BJH, et al. Intestinal microbiota and diabetic kidney diseases: the role of microbiota and derived metabolites inmodulation of renal inflammation and disease progression. *Best Pract Res Clin Endocrinol Metab*. 2021;35(3):101484. https://doi.org/10.1016/j.beem.2021.101484.
9 Chen YQ, Yang C, Deng ZH, et al. Gut microbially produced tryptophan metabolite melatonin ameliorates osteoporosis *via* modulating SCFA and TMAO metabolism. *J Pineal Res*. 2024;76(3):e12954. https://doi.org/10.1111/jpi.12954.
10 Dambrova M, Latkovskis G, Kuka J, et al. Diabetes is associated with higher trimethylamine *N*-oxide plasma levels. *Exp Clin Endocrinol Diabetes*. 2016;124(4):251-256. https://doi.org/10.1055/s-0035-1569330.
11 Guertin KA, Li XS, Graubard BI, et al. Serum trimethylamine *N*-oxide, carnitine, choline, and betaine in relation to colorectal cancer risk in the alpha tocopherol, beta carotene cancer prevention study. *Cancer Epidemiol Biomarkers Prev*. 2017;26(6):945-952. https://doi.org/10.1158/1055-9965.EPI-16-0948.
12 Kong LJ, Zhao QJ, Jiang XJ, et al. Trimethylamine *N*-oxide impairs beta-cell function and glucose tolerance. *Nat Commun*. 2024;15(1):2526. https://doi.org/10.1038/s41467-024-46829-0.
13 Wu P, Chen JN, Chen JJ, et al. Trimethylamine *N*-oxide promotes $ApoE^{(-/-)}$ mice atherosclerosis by inducing vascular endothelial cell pyroptosis *via* the SDHB/ROS pathway. *J Cell Physiol*. 2020;235(10):6582-6591. https://doi.org/10.1002/jcp.29518.
14 Zhou W, Cheng Y, Zhu P, et al. Implication of gut microbiota in cardiovascular diseases. *Oxid Med Cell Longev*. 2020;2020:5394096. https://doi.org/10.1155/2020/5394096.
15 Friedman JR, Nunnari J. Mitochondrial form and function. *Nature*. 2014;505(7483):335-343. https://doi.org/10.1038/nature12985.
16 Russell OM, Gorman GS, Lightowlers RN, et al. Mitochondrial diseases: hope for the future. *Cell*. 2020;181(1):168-188. https://doi.org/10.1016/j.cell.2020.02.051.
17 Miyamoto S, Zhang G, Hall D, et al. Restoring mitochondrial superoxide levels with elamipretide (MTP-131) protects db/db mice against progression of diabetic kidney disease. *J Biol Chem*. 2020;295(21):7249-7260. https://doi.org/10.1074/jbc.RA119.011110.
18 Takagi S, Li J, Takagaki Y, et al. Ipragliflozin improves mitochondrial abnormalities in renal tubules induced by a high-fat diet. *J Diabetes Investig*. 2018;9(5):1025-1032. https://doi.org/10.1111/jdi.12802.
19 Yao L, Liang XH, Liu YM, et al. Non-steroidal mineralocorticoid receptor antagonist finerenone ameliorates mitochondrial dysfunction *via* PI3K/Akt/eNOS signaling pathway in diabetic tubulopathy. *Redox Biol*. 2023;68:102946. https://doi.org/10.1016/j.redox.2023.102946.
20 Ma K, Chen G, Li W, et al. Mitophagy, mitochondrial homeostasis, and cell fate. *Front Cell Dev Biol*. 2020;8:467. https://doi.org/10.3389/fcell.2020.00467.
21 Shin JH, Kim KM, Jeong JU, et al. Nrf2-Heme oxygenase-1 attenuates high-glucose-induced epithelial-to-mesenchymal transition of renal tubule cells by inhibiting ROS-mediated PI3K/Akt/GSK-3β signaling. *J Diabetes Res*. 2019;2019:2510105. https://doi.org/10.1155/2019/2510105.
22 Sun MY, Ye HJ, Zheng C, et al. Astragalin ameliorates renal injury in diabetic mice by modulating mitochondrial quality control *via* AMPK-dependent PGC1α pathway. *Acta Pharmacol Sin*. 2023;44(8):1676-1686. https://doi.org/10.1038/s41401-023-01064-z.
23 Zhang G, Zhang J, DeHoog RJ, et al. DESI-MSI and METASPACE indicates lipid abnormalities and altered mitochondrial membrane components in diabetic renal proximal tubules. *Metabolomics*. 2020;16(1):11. https://doi.org/10.1007/s11306-020-1637-8.
24 Yu P, Zhang X, Liu N, et al. Pyroptosis: mechanisms and diseases. *Signal Transduct Target Ther*. 2021;6(1):128. https://doi.org/10.1038/s41392-021-00507-5.
25 Dai Z, Liu WC, Chen XY, et al. Gasdermin D-mediated pyroptosis: mechanisms, diseases, and inhibitors. *Front Immunol*. 2023;14:1178662. https://doi.org/10.3389/fimmu.2023.1178662.
26 Ding HY, Li JX, Li Y, et al. MicroRNA-10 negatively regulates inflammation in diabetic kidney *via* targeting activation of the NLRP3 inflammasome. *Mol Ther*. 2021;29(7):2308-2320. https://doi.org/10.1016/j.ymthe.2021.03.012.
27 Wang MZ, Wang J, Cao DW, et al. Fucoidan alleviates renal fibrosis in diabetic kidney disease *via* inhibition of NLRP3 inflammasome-mediated podocyte pyroptosis. *Front Pharmacol*. 2022;13:790937. https://doi.org/10.3389/fphar.2022.790937.
28 Al Mamun A, Ara Mimi A, Wu Y, et al. Pyroptosis in diabetic nephropathy. *Clin Chim Acta*. 2021;523:131-143. https://doi.org/10.1016/j.cca.2021.09.003.
29 Han JR, Zuo ZK, Shi XJ, et al. Hirudin ameliorates diabetic nephropathy by inhibiting Gsdmd-mediated pyroptosis. *Cell Biol Toxicol*. 2023;39(3):573-589. https://doi.org/10.1007/s10565-021-09622-z.
30 Yang SK, Han YC, He JR, et al. Mitochondria targeted peptide SS-31 prevent on cisplatin-induced acute kidney injury *via* regulating mitochondrial ROS-NLRP3 pathway. *Biomed Pharmacother*. 2020;130:110521. https://doi.org/10.1016/j.biopha.2020.110521.
31 Zhu DJ, Zhong J, Gong XF, et al. Augmenter of liver regeneration reduces mitochondria-derived ROS and NLRP3 inflammasome activation through PINK1/Parkin-mediated mitophagy in ischemia-reperfusion-induced renal tubular injury. *Apoptosis*. 2023;28(3-4):335-347. https://doi.org/10.1007/s10495-022-01794-1.
32 Wang K, Yao Y, Zhu X, et al. Amyloid β induces NLRP3 inflammasome activation in retinal pigment epithelial cells *via* NADPH oxidase- and mitochondria-dependent ROS production. *J Biochem Mol Toxicol*. 2017;31(6):21887. https://doi.org/10.1002/jbt.21887.
33 Deng LC, Shi CR, Li R, et al. The mechanisms underlying Chinese medicines to treat inflammation in diabetic kidney disease. *J Ethnopharmacol*. 2024;333:118424. https://doi.org/10.1016/j.jep.2024.118424.
34 Guo MF, Gao JR, Jiang L, et al. Astragalus polysaccharide ameliorates renal inflammatory responses in a diabetic nephropathy by suppressing the TLR4/NF-κB pathway. *Drug Des Devel Ther*. 2023;17:2107-2118. https://doi.org/10.2147/DDDT.S411211.
35 Feng HY, Wang YQ, Yang J, et al. Anthraquinones from *Rheum officinale* ameliorate renal fibrosis in acute kidney injury and chronic kidney disease. *Drug Des Devel Ther*. 2025;19:5739-5760. https://doi.org/10.2147/DDDT.S521265.
36 Tang D, He WJ, Zhang ZT, et al. Protective effects of Huang-Lian-Jie-Du Decoction on diabetic nephropathy through regulating AGEs/RAGE/Akt/Nrf2 pathway and metabolic profiling in db/db mice. *Phytomedicine*. 2022;95:153777. https://doi.org/10.1016/j.phymed.2021.153777.
37 Yu WX, Zeng CC, Wang CG, et al. N1F (Improved-Nephropathy 1 Formula) ameliorates renal interstitial fibrosis *via* inhibiting extracellular matrix deposition and regulating the FGF23/P38MAPK/Wnt pathway. *Cell Biochem Biophys*. 2024;82(2):927-943. https://doi.org/10.1007/s12013-024-01244-6.
38 Tanaka S, Sugiura Y, Saito H, et al. Sodium-glucose cotransporter 2 inhibition normalizes glucose metabolism and suppresses oxidative stress in the kidneys of diabetic mice. *Kidney Int*. 2018;94(5):912-925. https://doi.org/10.1016/j.kint.2018.04.025.
39 Liu BH, Wang DJ, Cao YW, et al. MitoTEMPO protects against podocyte injury by inhibiting NLRP3 inflammasome *via* PINK1/Parkin pathway-mediated mitophagy. *Eur J Pharmacol*. 2022;929:175136. https://doi.org/10.1016/j.ejphar.2022.175136.
40 Lin QS, Li S, Jiang N, et al. Inhibiting NLRP3 inflammasome attenuates apoptosis in contrast-induced acute kidney injury through the upregulation of HIF1A and BNIP3-mediated mitophagy. *Autophagy*. 2021;17(10):2975-2990. https://doi.org/10.1080/15548627.2020.1848971.
41 Yi ZY, Peng YJ, Hui BP, et al. Zuogui-Jiangtang-Yishen Decoction prevents diabetic kidney disease: intervene pyroptosis induced by trimethylamine *N*-oxide through the mROS-NLRP3 axis. *Phytomedicine*. 2023;114:154775. https://doi.org/10.1016/j.phymed.2023.154775.
42 Tang WH, Wang Z, Kennedy DJ, et al. Gut microbiota-dependent trimethylamine *N*-oxide (TMAO) pathway contributes to both development of renal insufficiency and mortality risk in chronic kidney disease. *Circ Res*. 2015;116(3):448-455. https://doi.org/10.1161/CIRCRESAHA.116.305360.
43 Yuk JM, Silwal P, Jo EK. Inflammasome and mitophagy connection in health and disease. *Int J Mol Sci*. 2020;21(13):4714. https://doi.org/10.3390/ijms21134714.
44 Todesca LM, Gerke M, Bulk EE, et al. Targeting $K_{(Ca)}3.1$ channels to overcome erlotinib resistance in non-small cell lung cancer cells. *Cell Death Discov*. 2024;10(1):2. https://doi.org/10.1038/s41420-023-01776-5.
45 Zeng C, Lin J, Zhang KT, et al. SHARPIN promotes cell proliferation of cholangiocarcinoma and inhibits ferroptosis *via* p53/SLC7A11/GPX4 signaling. *Cancer Sci*. 2022;113(11):3766-3775. https://doi.org/10.1111/cas.15531.

46 Bennett BJ, De Aguiar Vallim TQ, Wang Z, et al. Trimethylamine-*N*-oxide, a metabolite associated with atherosclerosis, exhibits complex genetic and dietary regulation. *Cell Metab*. 2013;17(1):49-60. https://doi.org/10.1016/j.cmet.2012.12.011.

47 Wang Z, Bergeron N, Levison BS, et al. Impact of chronic dietary red meat, white meat, or non-meat protein on trimethylamine *N*-oxide metabolism and renal excretion in healthy men and women. *Eur Heart J*. 2019;40(7):583-594. https://doi.org/10.1093/eurheartj/ehy799.

48 Lee JH, Lee JH, Kim KH, et al. Antibiotic-induced intestinal microbiota depletion can attenuate the acute kidney injury to chronic kidney disease transition *via* NADPH oxidase 2 and trimethylamine-*N*-oxide inhibition. *Kidney Int*. 2024;105(6):1239-1253. https://doi.org/10.1016/j.kint.2024.01.040.

49 Rath S, Heidrich B, Pieper DH, et al. Uncovering the trimethylamine-producing bacteria of the human gut microbiota. *Microbiome*. 2017;5(1):54. https://doi.org/10.1186/s40168-017-0271-9.

50 Li J, Zhao FQ, Wang YD, et al. Gut microbiota dysbiosis contributes to the development of hypertension. *Microbiome*. 2017;5(1):14. https://doi.org/10.1186/s40168-016-0222-x.

51 Shi Q, Nong K, Vandvik PO, et al. Benefits and harms of drug treatment for type 2 diabetes: systematic review and network meta-analysis of randomised controlled trials. *BMJ*. 2023;381:e074068. https://doi.org/10.1136/bmj-2022-074068.

52 Zhao TT, Zhang HJ, Yin XB, et al. Tangshen Formula modulates gut microbiota and reduces gut-derived toxins in diabetic nephropathy rats. *Biomed Pharmacother*. 2020;129:110325. https://doi.org/10.1016/j.biopha.2020.110325.

53 Tian E, Wang F, Zhao L, et al. The pathogenic role of intestinal flora metabolites in diabetic nephropathy. *Front Physiol*. 2023;14:1231621. https://doi.org/10.3389/fphys.2023.1231621.

54 Liu JJ, Liu S, Zheng H, et al. Urine tricarboxylic acid cycle metabolites and risk of end-stage kidney disease in patients with type 2 diabetes. *J Clin Endocrinol Metab*. 2025;110(2):e321-e329. https://doi.org/10.1210/clinem/dgae199.

55 Zhang XX, Chen JC, Lin RH, et al. Lactate drives epithelial-mesenchymal transition in diabetic kidney disease *via* the H3K14la/KLF5 pathway. *Redox Biol*. 2024;75:103246. https://doi.org/10.1016/j.redox.2024.103246.

56 Dong XX, Fu J, Yin XB, et al. Emodin: a review of its pharmacology, toxicity and pharmacokinetics. *Phytother Res*. 2016;30(8):1207-1218. https://doi.org/10.1002/ptr.5631.

57 Kong XR, Zhao YY, Wang XY, et al. Loganin reduces diabetic kidney injury by inhibiting the activation of NLRP3 inflammasome-mediated pyroptosis. *Chem Biol Interact*. 2023;382:110640. https://doi.org/10.1016/j.cbi.2023.110640.

58 Zhou YY, Gao CF, Vong CT, et al. Rhein regulates redox-mediated activation of NLRP3 inflammasomes in intestinal inflammation through macrophage-activated crosstalk. *Br J Pharmacol*. 2022;179(9):1978-1997. https://doi.org/10.1111/bph.15773.

59 Li DY, Xu WL, He SH, et al. Scutellarin inhibits pyroptosis *via* selective autophagy degradation of p30/GSDMD and suppression of ASC oligomerization. *Pharmacol Res*. 2025;212:107605. https://doi.org/10.1016/j.phrs.2025.107605.

60 Nishikawa T, Brownlee M, Araki E. Mitochondrial reactive oxygen species in the pathogenesis of early diabetic nephropathy. *J Diabetes Investig*. 2015;6(2):137-139. https://doi.org/10.1111/jdi.12258.

61 Sun SN, Yang SR, Cheng Y, et al. Jinlida Granules alleviate podocyte apoptosis and mitochondrial dysfunction *via* the AMPK/PGC-1α pathway in diabetic nephropathy. *Int J Mol Med*. 2025;55(2):26. https://doi.org/10.3892/ijmm.2024.5467.

62 Li QW, Liao JZ, Chen WJ, et al. NAC alleviative ferroptosis in diabetic nephropathy *via* maintaining mitochondrial redox homeostasis through activating SIRT3-SOD2/Gpx4 pathway. *Free Radic Biol Med*. 2022;187:158-170. https://doi.org/10.1016/j.freeradbiomed.2022.05.024.

63 Zhao DJ, Du BH, Xu JH, et al. Baicalin promotes antibacterial defenses by modulating mitochondrial function. *Biochem Biophys Res Commun*. 2022;621:130-136. https://doi.org/10.1016/j.bbrc.2022.06.084.

64 Sheng N, Zhang ZH, Zheng H, et al. Scutellarin rescued mitochondrial damage through ameliorating mitochondrial glucose oxidation *via* the Pdk-Pdc axis. *Adv Sci (Weinh)*. 2023;10(32):e2303584. https://doi.org/10.1002/advs.202303584.

65 Guo YJ, Zhang H, Yan C, et al. Small molecule agonist of mitochondrial fusion repairs mitochondrial dysfunction. *Nat Chem Biol*. 2023;19(4):468-477. https://doi.org/10.1038/s41589-022-01224-y.

66 Gavish L, Gilon D, Beeri R, et al. Photobiomodulation and estrogen stabilize mitochondrial membrane potential in angiotensin-II challenged porcine aortic smooth muscle cells. *J Biophotonics*. 2021;14(1):e202000329. https://doi.org/10.1002/jbio.202000329.

67 Oikawa Y, Izumi R, Koide M, et al. Mitochondrial dysfunction underlying sporadic inclusion body myositis is ameliorated by the mitochondrial homing drug MA-5. *PLoS One*. 2020;15(12):e0231064. https://doi.org/10.1371/journal.pone.0231064.

68 Perry RJ, Peng L, Barry NA, et al. Acetate mediates a microbiome-brain-beta-cell axis to promote metabolic syndrome. *Nature*. 2016;534(7606):213-217. https://doi.org/10.1038/nature18309.

69 Shang Y, Khafipour E, Derakhshani H, et al. Short term high fat diet induces obesity-enhancing changes in mouse gut microbiota that are partially reversed by cessation of the high fat diet. *Lipids*. 2017;52(6):499-511. https://doi.org/10.1007/s11745-017-4253-2.

70 Fu JF, Wang YT, Tan SM, et al. Effects of banana resistant starch on the biochemical indexes and intestinal flora of obese rats induced by a high-fat diet and their correlation analysis. *Front Bioeng Biotechnol*. 2021;9:575724. https://doi.org/10.3389/fbioe.2021.575724.

71 Li ZH, Weng J, Yan J, et al. Puerarin alleviates atherosclerosis *via* the inhibition of *Prevotella copri* and its trimethylamine production. *Gut microbiota*. 2024;73(12):1934-1943. https://doi.org/10.1136/gutjnl-2024-331880.

72 She JQ, Tuerhongjiang G, Guo MY, et al. Statins aggravate insulin resistance through reduced blood glucagon-like peptide-1 levels in a microbiota-dependent manner. *Cell Metab*. 2024;36(2):408-421.e5. https://doi.org/10.1016/j.cmet.2023.12.027.

73 Wang H, Rong X, Zhao G, et al. The microbial metabolite trimethylamine *N*-oxide promotes antitumor immunity in triple-negative breast cancer. *Cell Metab*. 2022;34(4):581-594.e8. https://doi.org/10.1016/j.cmet.2022.02.010.

74 Zhou XF, Zhang BW, Zhao XL, et al. Chlorogenic acid prevents hyperuricemia nephropathy *via* regulating TMAO-related gut microbes and inhibiting the PI3K/AKT/mTOR pathway. *J Agric Food Chem*. 2022;70(33):10182-10193. https://doi.org/10.1021/acs.jafc.2c03099.

75 Zhang XN, Shi L, Chen R, et al. Chlorogenic acid inhibits trimethylamine-*N*-oxide formation and remodels intestinal microbiota to alleviate liver dysfunction in high L-carnitine feeding mice. *Food Funct*. 2021;12(21):10500-10511. https://doi.org/10.1039/d1fo01778k.